Journal of Materials Processing Tech. 336 (2025) 118699

Contents lists available at ScienceDirect

Journal of Materials Processing Tech.

journal homepage: www.elsevier.com/locate/jmatprotec

Research article

Curvature, microstructure, and mechanical property of an asymmetric aluminium profile produced by sideways extrusion with variable speed

Jiaxin Lv [a], Xiaochen Lu [a], Junquan Yu [b,*], Zhusheng Shi [a,*], Jianguo Lin [a,c]

[a] Department of Mechanical Engineering, Imperial College London, London SW7 2AZ, UK
[b] Key Laboratory for Liquid-Solid Structural Evolution and Processing of Materials (Ministry of Education), Shandong University, Jinan, Shandong 250061, PR China
[c] Department of Industrial and Systems Engineering, The Hong Kong Polytechnic University, Hung Hom, Kowloon, Hong Kong

ARTICLE INFO

Keywords:
Sideways extrusion
Microstructure
Weld quality
Deformation characterisation
Aluminium profile

ABSTRACT

Sideways extrusion is an advanced technology for one-step production of curved profiles eliminating the need for subsequent bending processes. Its effectiveness in controlling the bending curvature of symmetric products has been well established in prior research. However, there is no report on the effect of asymmetric product shape on bending curvature and still lacking quantitative analysis of welding quality and microstructure of the extrudate for the sideways extrusion, limiting its application scope. In this study, an asymmetric Z-shape aluminium profile was manufactured using sideways extrusion at different speeds and the corresponding numerical simulation was conducted to analyse the extrudate shape, welding quality, microstructural and mechanical properties. The bending mechanism of extrudate, resulting from the non-uniform metal flow during extrusion, was identified. The curvature radius was found to depend on the average exit velocity and the velocity gradient along the transverse direction both of which increase with increasing extrusion speed. Improvements in welding quality and increased recrystallisation fraction during extrusion were quantitatively predicted using developed subroutines and these predications aligned well with the results from post-extrusion examination. In addition, tensile test results differed for profile sections extruded at different speeds, which were attributed to the combined effect of welding quality, work hardening, recovery and continuous dynamic recrystallisation.

1. Introduction

Extruded aluminium profiles have been increasingly used for lightweight application thanks to the high specific strength of aluminium and the high capability of producing complex cross-sections during extrusion process [1]. The United Nations has released 17 goals of sustainable development, including ensuring sustainable production patterns and taking urgent action to combat climate change [2]. Many research efforts have been made on aluminium extrusion technology to align with these goals. For example, multi-container extrusion [3], spread extrusion [4] and flat extrusion [5] methods can effectively reduce force requirement and extend the geometrical limit of extrusion products. Continuous extrusion forming method offers higher productivity and efficiency in producing long profiles with minimal material waste [6]. Friction extrusion [7] and shear assisted processing and extrusion [8] methods can enhance the property of extrudate and offer the potential to recycle aluminium chips. Extrusion with warm bending method [9] allows for the creation of severely curved profiles with reduced springback.

Under the backdrop of advancing the sustainable development, sideways extrusion technique has been proposed by Zhou et al. [10] for directly manufacturing curved profiles in a single extrusion operation, eliminating the need of subsequent bending operation. In sideways extrusion process, two punches move simultaneously toward each other in the extrusion die and push the material to exit from lateral die orifice. By adjusting the velocities of these two individual punches variable extrudate curvature can be obtained, which has been provided theoretically, experimentally, and numerically [11]. The deformation mechanisms and its induced microstructural evolution inside the die during sideways extrusion process was characterised and compared with conventional forward extrusion [12]. To date, most of the related research is based on the extrusion of round bars or tubes which have a simple and symmetric cross-section, where uniform material flow can be achieved easily.

The extrusion of asymmetric cross-sections typically requires asymmetric tooling structures, leading to non-uniform metal flow [13]. This

* Corresponding authors.
E-mail addresses: junquan.yu@sdu.edu.cn (J. Yu), zhusheng.shi@imperial.ac.uk (Z. Shi).

https://doi.org/10.1016/j.jmatprotec.2024.118699
Received 6 November 2024; Received in revised form 4 December 2024; Accepted 16 December 2024
Available online 18 December 2024

non-uniformity ultimately results in difficulty in achieving accurate shapes with respect to the target profiles. For conventional extrusion of straight asymmetric profiles, various tooling optimisation methods have been successfully employed to enhance the uniformity of metal flow. These methods encompass adjustments in bearing length distribution [14], optimisation of porthole dimensions and configurations [15,16], and the embedment of baffles in the welding chamber [17]. Conversely, an alternative research direction seeks to leverage the non-uniformity resulting from asymmetry to directly produce curved profiles. Dajda et al. [18] proposed a method for extruding pipe elbows by employing an eccentrically mounted mandrel, which creates asymmetric friction between the container and billets, leading to the non-uniform metal flow. This approach generates curved profiles due to the uneven distribution of metal exit velocities at the die orifice. Kowalik et al. [19] further presented that the degree of extrusion curvature is significantly influenced by the asymmetry of the tooling structure. Min et al. [20,21] demonstrated that even to produce symmetric profiles, the bending curvature can be achieved by introducing asymmetric metal flow zones in the extrusion tool, such as asymmetric deflectors and distorted streamlined channels. Zhou et al. [12] utilised sideways extrusion to produce asymmetric profiles and found that, despite the velocities of both punches being identical, the extruded profile still exhibited curvature. However, as an advanced technology for producing curved profiles, sideways extrusion has yet to be investigated regarding the curvature control of asymmetric profiles.

In sideways extrusion, like in conventional extrusion methods, welds are inevitably formed during the production of hollow profiles [22]. Furthermore, even for solid profiles, the billet of sideways extrusion is typically cut to two pieces for the convenient insertion of the material into the opposite containers, resulting in the welds during the bonding between the materials from the two billets. To date, only one literature [23] addresses the weld formation mechanism in sideways extrusion of round bars, and no evaluation of welding quality has been conducted for this process. Based on the welding evaluation for traditional extrusion, an unsound welding interface can significantly deteriorate the property in welding zone, resulting in the poor mechanical quality of extrudate, while a sound weld allows extrudate to obtain a mechanical property mainly decided by microstructures [24]. The quality of extrusion weld depends on three key factors, namely welding pressure, temperature, and extrusion speed [25]. Increasing pressure enhances welding quality, leading to a sound weld with mechanical properties comparable to the matrix material [26]. Yu et al. [27] has conducted a series of experiments and simulations and showed that increasing both temperature and speed is favourable for good welding quality of welds that leads to high ultimate tensile strength and elongation. These two factors, i.e. extrusion temperature and speed, not only promote the closure of the micro-voids between the bonding interfaces, but also contribute to the generation of new grains through the bonding interface. However, some conflicting conclusions have also been reported regarding the effect of extrusion speed. Gagliardi et al. [28] found that increasing extrusion speed reduces the overall pressure in the welding chamber, resulting the reduced ductility of extrudate. Donati et al. [29] arrived at the same conclusion by plotting the variation of fracture elongation as a function of extrusion speed based on numerous tensile testing data.

The microstructural evolution during sideways extrusion at different speeds is still not clear, although it has been extensively analysed during conventional extrusion. In traditional extrusion, microstructural evolution usually occurs during hot extrusion following dynamic recovery, dynamic recrystallisation (DRX), and grain growth mechanisms [30,31]. Beyond merely acting as a softening mechanism that consumes dislocations and reduces hot deformation resistance, DRX also plays a pivotal role in grain refinement, which in turn enhances the mechanical properties of metals [32]. Numerous reports in the literature have highlighted that the fraction of DRX is highly contingent on both the strain level and strain rate during the metal forming process [33]. Under a constant strain rate, increasing the strain to a critical threshold is imperative for the initiation of DRX, and a higher strain level leads to a more pronounced degree of DRX [34]. Conversely, under a constant strain level, elevating the strain rate significantly inhibits the formation of new grains due to the limited time available for energy accumulation [35]. In the context of the extrusion process, both strain and strain rate within the material vary across different positions and continuously evolve as the extrusion progresses. Lin et al. [36] found that during extrusion process of 2099 Al-Li alloy, DRX preferentially occurred in the surface layer due to the friction induced high strain, by which new grains can form with a few seconds and then start to grow. Fan et al. [37] investigated the grain morphology history along the forming path of porthole extrusion and found recrystallisation happened where grains were elongated inside the die and pinched off when exiting from the die orifice. The extrusion parameters influencing the microstructure of extruded profile include extrusion ratio and extrusion speed since they can directly determine the overall effective strain $\bar{\varepsilon}$ and strain rate ($\dot{\varepsilon}$) of the material during extrusion. Kaneko et al. [38] studied the microstructure changes after extrusion of Al-Mg-Si-Cu alloy at 480 °C. The results showed that the average grain size decreased from 24.6 μm at the extrusion ratio of 4.6 ($\bar{\varepsilon} = 1.5$) to 13.4 μm at the extrusion ratio of 256 ($\bar{\varepsilon} = 3.2$), indicating that high strain can facilitate DRX and grain refinement. The author also found that increasing extrusion speed from 0.67 mm/s to 2.67 mm/s led to the decrease of grain size at a low effective strain ($\bar{\varepsilon} = 1.5$) while an opposite phenomenon was observed at a high effective strain ($\bar{\varepsilon} = 3.2$). Chen et al. [39] investigated the microstructure of 2196 Al-Li alloy extrusions, uncovering a non-linear relationship between extrusion speed and microstructure. As extrusion speed rose from 0.1 mm/s to 0.5 mm/s, a reduction in average grain size was observed, indicating enhanced DRX. However, a further increase in speed from 0.5 mm/s to 1 mm/s resulted in a slight increase in grain size. This contrasting impact of higher extrusion speeds can be primarily attributed to the interplay of different mechanisms: while high extrusion speed increases the strain rate, which tends to inhibit DRX, it also elevates the temperature, thereby facilitating DRX.

Although some studies on sideways extrusion and extrusion welding have been made, there are still three critical research gaps. Firstly, previous studies on sideways extrusion have solely attributed the bending of the extrudate to the extrusion speed ratio, i.e. the difference between the upper and lower punches. The effect of profile shape on curvature has not been considered, which can significantly restrict the applicability of sideways extrusion, especially in producing profiles with asymmetric cross-sections. Secondly, although one previous study [23] has examined the welding during sideways extrusion, it only focused on the material welding state inside the extrusion tool. The evaluation of the welding quality of the final extruded profile is rarely seen. This raises the question of whether the sideways extrusion method can form sound welds in final profiles, particularly in scenarios where welds are inevitable, such as in hollow profile extrusion. Thirdly, the effects of extrusion speed on welding quality and microstructural evolution during sideways extrusion are rarely studied or quantified. This study aims to address the afore-mentioned research gaps. In this research, sideways extrusion experiment was carried out to produce an asymmetric thin-walled Z-shape profile at various extrusion speeds. The velocities of the opposing punches were equated to ensure that the profile's curvature depends solely on the uniformity of metal flow, rather than on differential punch velocity. Optical microscopy (OM) observation, electron backscatter diffraction (EBSD), and tensile tests were conducted at the selected zones of extrudate which were extruded at different speeds. Finite element modelling, implemented by two user-defined subroutines regarding welding quality evaluation and DRX fraction, was performed in alignment with the sideways extrusion experiment to facilitate understanding of deformation features and the resulting extrudate properties.

2. Experiments and simulation of sideways extrusion process

2.1. Extrusion tool design

Fig. 1 illustrates the experimental set-up of the sideways extrusion system for a target profile. Fig. 1(a) shows the extrusion die manufactured from H13 tool steel in two halves for the ease of taking out the remaining material after extrusion. By assembling the dies together, a container can be formed across the height of the die set to host billets during extrusion and two punches, namely upper punch and lower punch, are able to move vertically through it, driven by hydraulic presses. The die set is supported by a platform where there is a central hole to enable the movement of the lower punch. The overall dimensions of the die set are 160 × 160 × 220 mm, and the diameter of the billet container is 12.6 mm. Six holes with a diameter of 10 mm and a length of 210 mm are situated inside each half die for hosting cartridge heaters to heat up the die set and billets to the desired temperature during extrusion process. Thermocouples were inserted into the die as shown in Fig. 1(a), with their tips positioned approximately 7 mm from the die inner wall for real-time temperature monitoring. Fig. 1(b) shows half of the 3D model of the sideways extrusion assembly, emphasising the die orifice on the middle area of the container lateral surface. Through the die orifice, the material of the billets can be deformed and exit as the given geometry with cross-sectional dimensions the same as the desired extrudate as shown in Fig. 1(c). The target extrudate is an asymmetric Z-shape profile composed with a top flange, bottom flange, and thin rib. The upper flange is 3.5 mm in width and 1.5 mm in height, while the bottom flange has a smaller cross-section with a width of 2.5 and a height of 2 mm. The thickness of the thin rib is 1 mm and overall extrudate height is 23.5 mm. The extrusion ratio, i.e. the ratio of cross-sectional area of the billets to the extrudate, can be calculated as 3.99, according to the geometry of the die set.

2.2. Experiment material, flow stress, and constitutive model

An as-received homogenised AA1070 pure aluminium ingot was machined into billets with a diameter of 12.5 mm and a length of 90 mm for the extrusion test in this study. In the initial billet, coarse grains with rare low angle boundaries (LABs) and dislocations were distributed with an average grain size of ~3 mm. Compression tests were conducted at various temperatures and strain rates using the Gleeble 3800 thermal-mechanical physical simulator. The detailed flow stress data is presented in Fig. 2. Generally, the flow stress exhibits a rapid increase due to work hardening, followed by a gradual decrease caused by dynamic recovery and recrystallisation. This pattern is consistent across different temperatures and strain rates although the specific stress values vary. To describe the effect of temperature, strain rate and strain on the flow stress, a nonlinear model [40,41] was used and the derived equation is given as follows:

$$\sigma = \frac{1}{0.9787}\ln\left\{\left(\frac{Z}{6.9193\times10^{8}}\right)^{\frac{1}{5.4027}} + \left[\left(\frac{Z}{6.9193\times10^{8}}\right)^{\frac{2}{5.4027}}+1\right]^{\frac{1}{2}}\right\} \times \frac{7000\varepsilon}{3+500\varepsilon^{1.08}} \tag{1}$$

where ε represents strain level and Z is Zener-Hollomon parameter that can be calculated with strain rate $\dot{\varepsilon}$ and temperature T, i.e. $Z = \dot{\varepsilon}\exp\left(\frac{143870}{T}\right)$. The predicted flow curves are plotted as solid lines in Fig. 2, showing a good agreement with the experimental results.

2.3. Experimental procedures

Before extrusion, the tools were assembled with billets inside the container, heating cartridges inside the heating holes and punches attached to the hydraulic presses. The whole system was then heated to a desired temperature and held for 20 minutes to ensure a uniform temperature distribution. During extrusion, the upper and lower punches were actuated simultaneously with the opposing motion (the upper one moved down and the lower one moved up) at a designed speed, forming a profile from the horizontal orifice of the die set. After extrusion, the extrudate was cut off and quenched immediately with room-temperature water.

In this study, the sideways extrusion tests were conducted where the stroke of each punch was 52 mm. The extrusion temperatures for both the billets and dies were set to 520 °C, in line with industrial extrusion practices. During extrusion, the die temperature was monitored in real-time via thermocouples and the heating system adjusted its efficiency based on these readings to maintain dynamic temperature equilibrium of the die around 520 °C. Both the upper and lower punches were moved at the same velocity, i.e. extrusion speed. The whole extrusion process can be divided into four stages according to the different extrusion speeds applied, i.e. 0.05, 0.1, 0.5 and 1 mm/s, respectively, during each of which, the punches were moved upward or downward for 13 mm. This means during the whole extrusion process, each billet was extruded

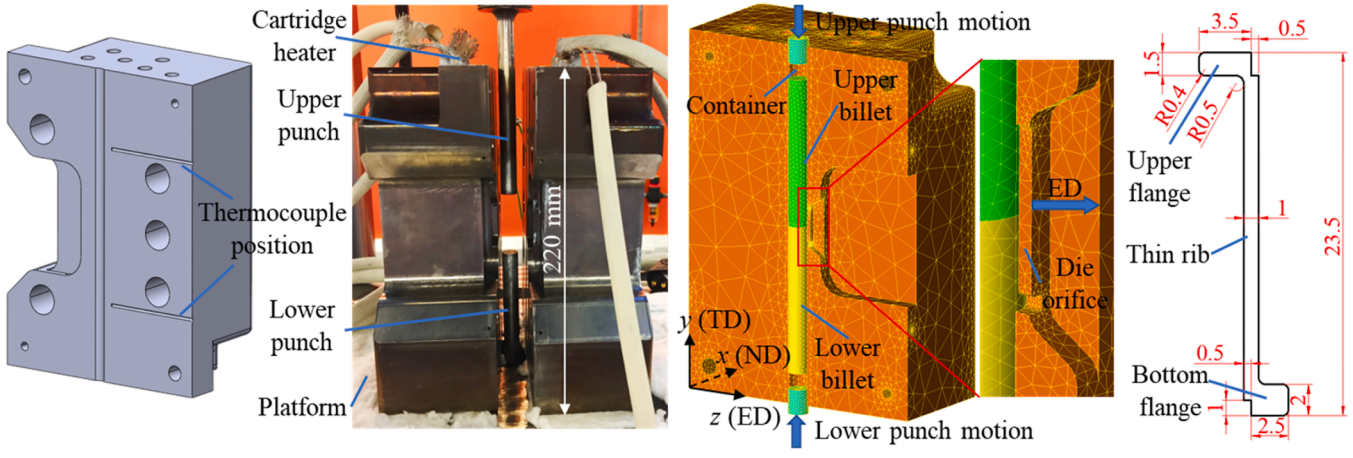

Fig. 1. Illustration of sideways extrusion system and cross-sectional dimensions of the extrudate (mm).

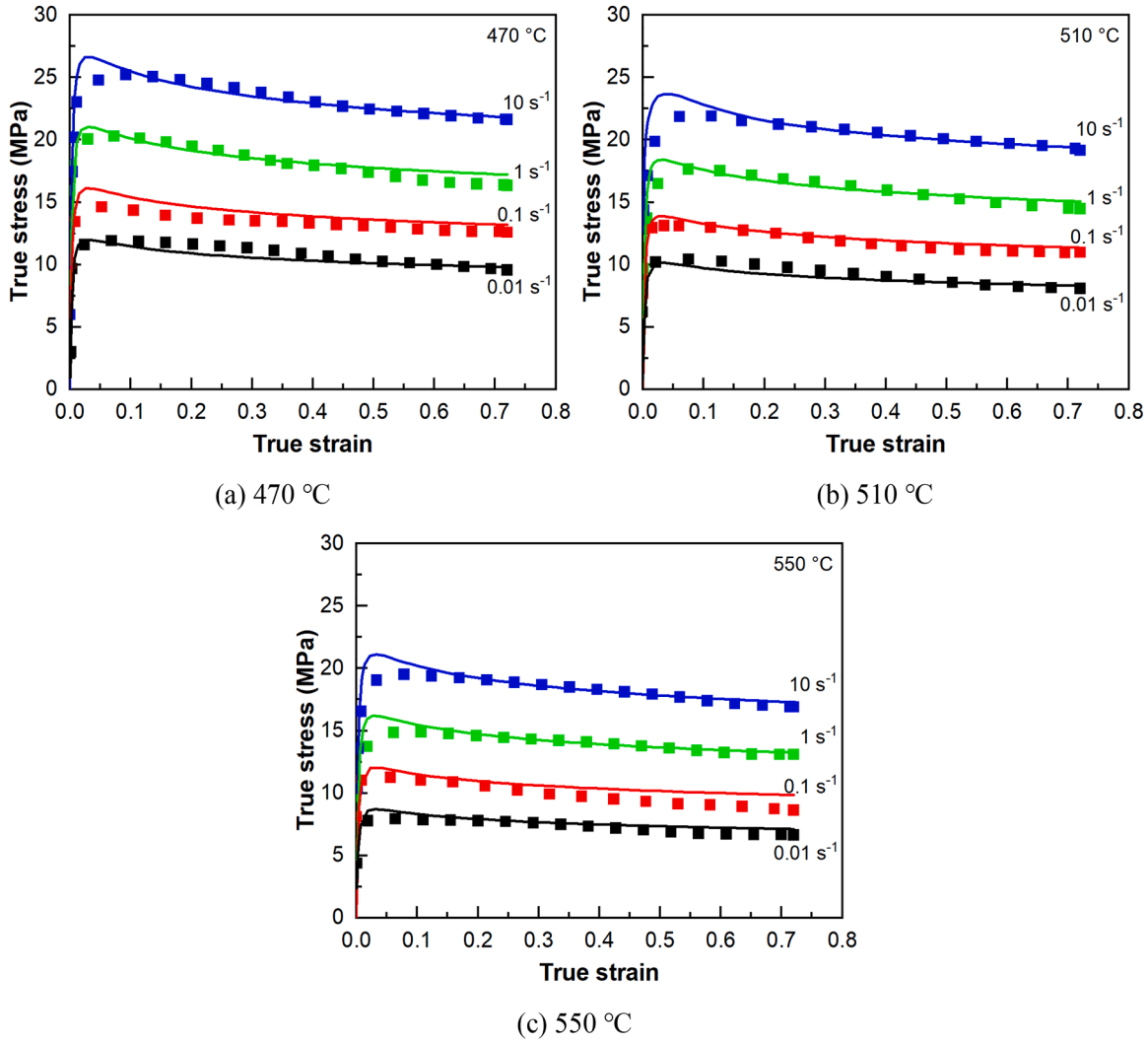

Fig. 2. Stress-strain curves of AA1070 at various strain rates and temperatures obtained from thermomechanical tests (symbols) and the corresponding model predictions (lines).

at an extrusion speed of 0.05 mm/s for the first 13 mm, then 0.1 mm/s for the second 13 mm, followed 0.5 mm/s for the third 13 mm, and finally 1 mm/s for the last 13 mm, with no pause in the middle. These various extrusion speeds were chosen according to previous research [10–12], aiming to study the effect of extrusion speed on welding quality, microstructure and mechanical property of the sideways extruded profile. The extrusion tests were repeated to ensure the reliability of the results, and one extrudate was used for further microstructural and mechanical examinations.

2.4. Numerical modelling

2.4.1. Numerical model establishment

Numerical simulation of the sideways extrusion process was conducted using Qform software for a better understanding of the metal flow and physical characteristics of sideways extrusion at different extrusion speeds. Fig. 1(b) shows half of the corresponding finite element (FE) model of the extrusion process, where the upper and lower punches were represented as two cylinders moving downward and upward, respectively, and two billets were inserted in the container of the die set with the contacting interface aligned with the centre of the die orifice. The coordinate system is defined as follows: the x-direction is parallel to the Normal Direction (ND), the y-direction to the Transverse Direction (TD), and the z-direction to the Extrusion Direction (ED). The billets and tools were automatically meshed into tetrahedron elements the size of which is controlled using adaption factor and an acceleration coefficient. The maximum value of the adaptation factor was set to 15, which ensures the size ratio of the biggest element to the smallest element does not exceed 15. The acceleration coefficient was defined as 1.5, limiting the size difference between neighbouring elements to be no greater than 1.5 times. Additionally, the maximum number of steps before remeshing was set to 20.

The materials applied in the FE simulation was the same as those in the experiment, i.e. AA1070 for billet and H13 tool steel for tools. The material properties summarised in Fig. 3 [42–46] and the stress-strain data in Section 2.2 were imported into Qform software.

The friction behaviour between the billets and die was simulated based on the Levanov friction law:

$$\tau = m\frac{\sigma}{\sqrt{3}}\left(1 - e^{-b\frac{\sigma_n}{\sigma}}\right) \tag{2}$$

where τ is the friction stress, m is the shear friction factor, b is the Levanov coefficient, σ is the flow stress and σ_n is the normal contact pressure. m was set to 1 to reflect that no lubricant was used between the billets and die, consistent with the extrusion tests. b was set to 1.25 as recommended by Levanov [47]. This setting allows the Levanov friction law to generalise both the Shear friction model and Coulomb friction

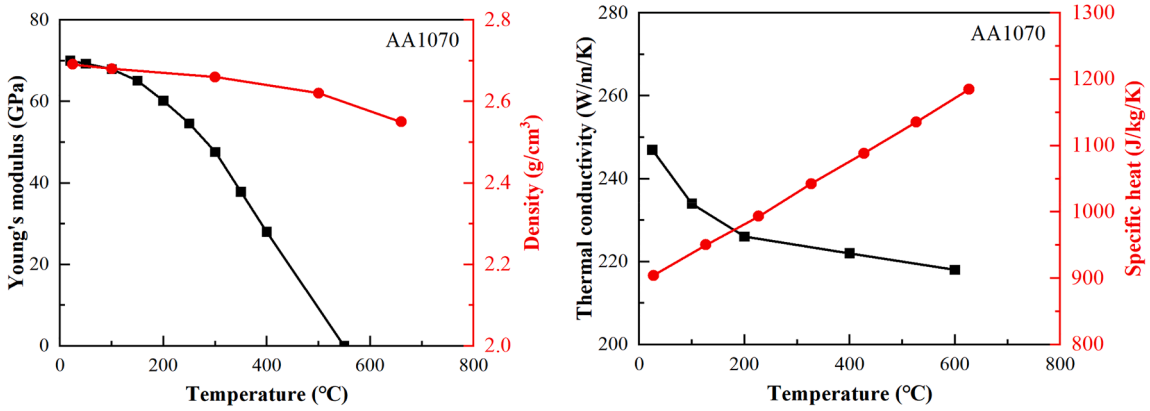

(a) Billet Young's modulus and density [42, 44] (b) Billet's thermal conductivity and specific heat [44, 45]

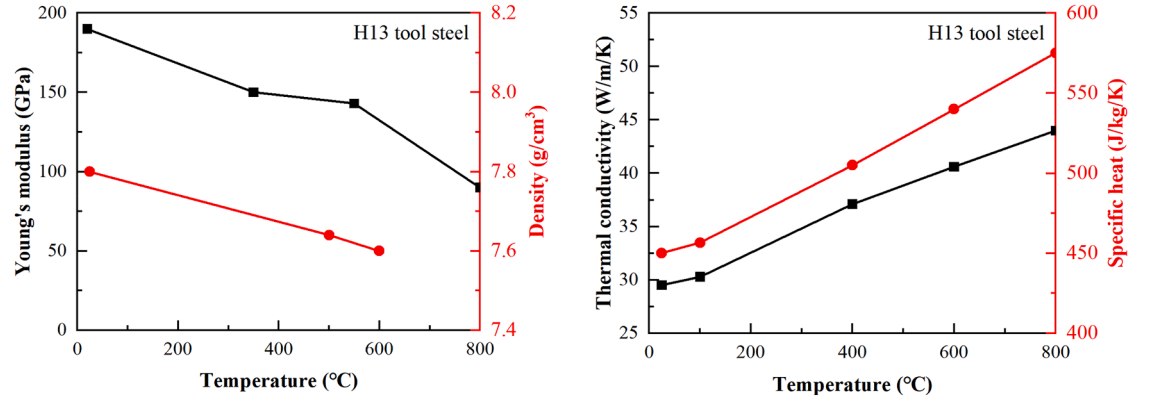

(c) Tool's Young's modulus and density [43, 46] (d) Tool's thermal conductivity and specific heat [43]

Fig. 3. Properties of the (a-b) billet material AA1070 and (c-d) tooling material H13 steel.

model, making the estimated friction force increase at a decreasing rate before reaching a plateau and thereby offering the most realistic predictions.

2.4.2. *Subroutines for simulating welding quality and recrystallisation fraction*

During the numerical simulations, two subroutines were incorporated to quantitatively assess the welding quality and the degree of recrystallisation. The welding quality was evaluated using the J criterion [48]:

$$J = \int k_0 \frac{|\sigma_m|}{\overline{\sigma}} \dot{\varepsilon} \exp\left(\frac{RT}{Q_d}\right) dt \tag{3}$$

where σ_m is the mean stress, $\overline{\sigma}$ is the effective stress, $\dot{\varepsilon}$ is the strain rate. T is the absolute temperature, R is the universal gas constant (8.314 J/(mol·K)), Q_d is the diffusion activation energy (1.42×10^5 J/mol), and $k_0 = 1$ is a coefficient related to the material and the surface conditions of the metal to be bonded. A higher J index indicates better welding quality. For the purpose of numerical simulation, Eq. (2) can be written into incremental form as:

$$J_n = J_{n-1} + \Delta J_n \tag{4}$$

where

$$\Delta J_n = k_0 \frac{|\sigma_{mn}|}{\overline{\sigma}_n} \dot{\varepsilon}_n \exp\left(\frac{RT_n}{Q_d}\right) \Delta t_n \tag{5}$$

The variables J_n and J_{n-1} are respectively the J value at simulation step n and $n-1$, and the initial J value before simulation is set to zero, i.e. $J_0 = 0$. ΔJ_n represents the increment of J at step n for each finite element. The terms σ_{mn}, $\overline{\sigma}_n$, and $\dot{\varepsilon}_n$ represent the mean stress, effective stress and strain rate value in the n^{th} simulation step. Δt_n is the incremental extrusion time covered in the n^{th} step. A user-defined subroutine was thus developed for the numerical simulation of J index, and its flowchart is shown in Fig. 4(a). The constants and J_0 are defined at first. Following this, for each simulation step n, set ΔJ_n to zero, then input related variables from of the last step (n-1) from the main program, calculate ΔJ_n if compressive stress is applied to the material ($\sigma_{mn} < 0$), and finally update J_{n+1} to the main program.

On the other hand, a conventional DRX kinetics model was utilised to estimate the DRX fraction during sideways extrusion. The parameters relevant to this model were determined using a methodology detailed in Ref [49], based on the stress-strain curves in Fig. 2. This finally led to the formulation of the DRX model as follows:

$$\begin{cases} X_{DRX} = 1 - \exp\left[-0.71014\left(\dfrac{\overline{\varepsilon} - \overline{\varepsilon}_c}{\overline{\varepsilon}_{0.5} - \overline{\varepsilon}_c}\right)^{1.8596}\right] (\overline{\varepsilon} \geq \overline{\varepsilon}_c) \\ \overline{\varepsilon}_{0.5} = 0.351621 Z^{0.0042} \\ \overline{\varepsilon}_c = 0.01104 Z^{0.0712} \\ Z = \dot{\varepsilon} \exp(Q_d / RT) \end{cases} \tag{6}$$

where X_{DRX} is the volume fraction of DRX, $\overline{\varepsilon}$ is the effective strain, $\overline{\varepsilon}_c$ signifies the critical strain beyond which DRX occurs, $\overline{\varepsilon}_{0.5}$ denotes the strain at which 50 % of DRX is completed, and Z corresponds to Zener-Hollomon parameter. To adapt Eq. (5) for numerical simulation, it was modified to calculate the DRX fraction for each element at the n^{th} step as

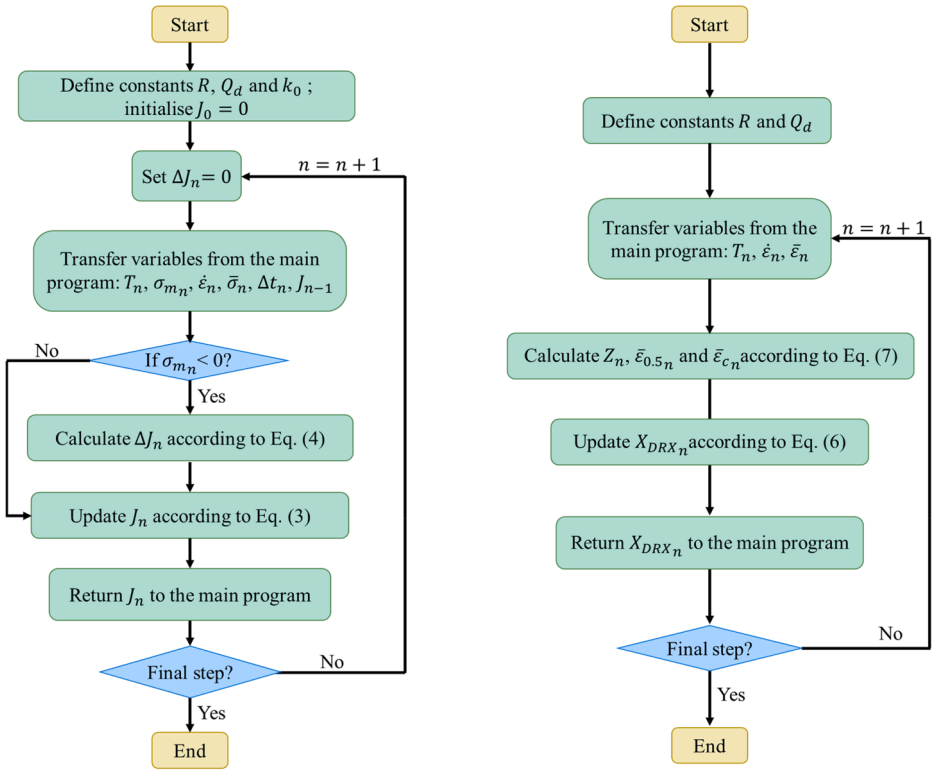

(a) J index for welding quality (b) X_{DRX} for recrystalisation fraction

Fig. 4. Flowcharts of the subroutines for numerical simulation of (a) J index for welding quality, and (b) X_{DRX} for recrystallisation fraction.

follow:

$$X_{DRX_n} = 1 - \exp\left[-0.83335\left(\frac{\bar{\varepsilon}_n - \bar{\varepsilon}_{cn}}{\bar{\varepsilon}_{0.5n} - \bar{\varepsilon}_{cn}}\right)^{1.4328}\right] \quad (\bar{\varepsilon}_n \geq \bar{\varepsilon}_{cn}) \tag{7}$$

where

$$\begin{cases} \bar{\varepsilon}_{0.5n} = 0.80228 Z_n^{\,0.0808} \\ \bar{\varepsilon}_{cn} = 0.00399 Z_n^{\,0.2341} \\ Z_n = \dot{\varepsilon}_n \exp(Q_d / RT_n) \end{cases} \tag{8}$$

According to Eqs. (6) and (7), the subroutine for calculating X_{DRX} is established as shown in Fig. 4(b).

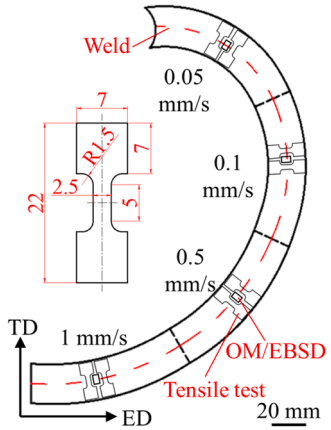

Fig. 5. Tensile specimen and sampling locations for post-extrusion examination.

2.5. Post examination of extrudate

Fig. 5 shows the schematic curved extrudate and sampling locations for further examination. Four small rectangle samples were prepared for microstructural observations, including both optical microscopy (OM) and electron backscatter diffraction (EBSD), located in the middle of each of the four sections extruded at different speeds. Adjacent to each small sample, two miniature dog bone-shape specimens were prepared for tensile tests, whose geometry and dimensions are shown in the centre of Fig. 5. These tensile testing specimens were used to evaluate the welding quality. They were cut in the direction perpendicular to the extrusion direction, and the positions were such that the welding seam was included in the tensile sample gauge length. All the tensile tests were conducted using an Instron servo-electric mechanical testing machine at room temperature with an extension speed of 0.04 mm/min, equivalent to a strain rate of around 0.00013 s^{-1}.

Both OM and EBSD observations were performed to investigate the microstructural characteristics on the mid flow plane ED-TD. For OM test, the four samples were prepared by metallographically grinding with SiC papers (800, 1200, 2500 and 4000 grit), polished with 50 nm OP-S (Oxide Polishing Suspensions) and then etched in the solution of Alpha Case regent for 10 minutes. After that, a Zeiss Axio Scope A1 microscope was used for OM observations and the Leica Application Suite software for OM image analysis. For EBSD analysis, the welds in the samples were initially identified based on the results from OM observations. Subsequently, the samples were re-ground using emery papers up to 4000 grit and re-polished with OP-S colloidal silica for 30 minutes. Following the sample preparation, EBSD measurements were performed using a Hitachi S-3400N SEM equipped with a Bruker's QUANTAX EBSD detector, operated at an accelerating voltage of 20 kV.

3. Results and discussion

3.1. Extrusion experimental results and validation of FE model

Fig. 6 shows the extruded profiles after two repeated sideways extrusions to verify the reliability of the experimental results. The shape is noticeably upward bending although the motion velocities of the upper punch and lower punch are the same during the whole extrusion process. Specifically, the curvature radii of the three extruded profiles were measured, showing the values of 94.8/93.2, 109.1/106.6, 120.6/117.1, and 169.2/167.5 mm for extrusion speed of 0.05, 0.1, 0.5, and 1 mm/s, respectively.

The extrusion force evolutions for the upper and lower punches are shown in Fig. 7(a) and (b), respectively, along with the results from numerical simulations for comparison. Initially, the extrusion force rapidly increases to the peak as the material breaks through the die orifice, then slightly decreases as extrusion progresses. At each speed transition from low to high, the force jumps to a higher level before gradually decreasing until the next transition. For the upper punch, the peak forces for the four speeds are 15.66, 17.01, 18.75, and 19.26 kN, respectively. The lower punch shows slightly lower forces, 15.14, 15.96, 17.82, and 19.19 kN for each speed, due to the upward curvature of the extrudate. Additionally, the simulation aligns well with experimental data, confirming the FE model's accuracy. It is also noted that, unlike the direct surge seen in simulation results, the experimental data show an initial drop followed by a force surge at each speed transition. This pattern corresponds to the brief pause in the hydraulic press operation required for the speed change.

3.2. Quantification of the effect of extrusion speed on extrudate curvature

The FE model was firstly validated by comparing the curved shape of the extruded profile obtained from the experiment and simulation. Fig. 8 (a) shows the simulated extrudates after the four speed stages of sideways extrusion. The shape of the simulated extrudate agrees well with the experimental results in Fig. 6, with the simulated curvature radii of 93.9, 98.9, 110.4, and 157.7 mm for each extrusion speed, respectively, indicating an error percentage between experiment and simulation within 10.9 %. The bending of extrudate can be attributed to the fact that the upper flange of the extrudate (3.5 × 1.5 mm) has a greater contact area with the inner wall of the die, resulting in higher metal flow resistance compared to the lower flange (2.5 × 2 mm), as depicted in Fig. 1(c). It can be seen that the curvature radius increases with the increasing extrusion speed. To quantify the effect of metal flow non-uniformity on the extrudate curvature, the schematic of material flow through the die orifice is shown in Fig. 8(b), with the y-axis representing TD and z-axis indicating ED. The exit velocity is assumed to vary linearly along y-axis with a consistent gradient k, which can be validated by the simulation results in Fig. 8(c). This variation of exit velocity leads to the curvature of extrudate, characterised by the curvature radius R_c and the bending angle $\Delta\theta$. Point O represents the middle point on the cross-section of the thin rib with a velocity denoted as v_m. Meanwhile, O_1 and O_2 are two arbitrary points, each having respective y-coordinates y_1 and y_2, with velocities of v_1 and v_2, respectively. Given a finite element time interval Δt, the points O_1 and O_2 move by Δz_1 and Δz_2, respectively, which can be calculated as:

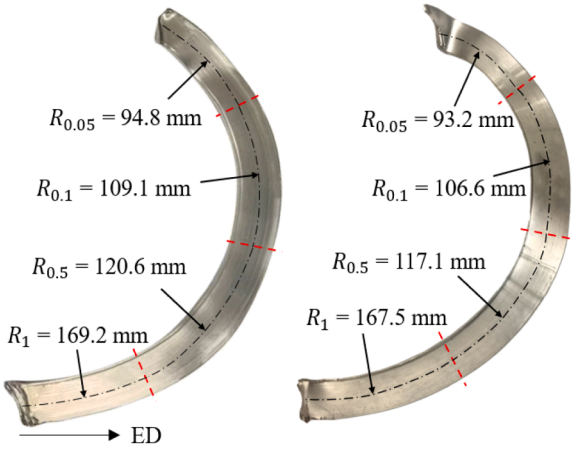

Fig. 6. Extruded profiles with marked curvature measurements after two repeated sideways extrusions.

$$\Delta z_1 = v_1 \Delta t \tag{9}$$

$$\Delta z_2 = v_2 \Delta t \tag{10}$$

Since the points O_1 and O_2 move along arcs, their actual movement lengths, denoted as Δs_1 and Δs_2 are approximately equal to Δz_1 and Δz_2, respectively, under the finite element condition. They can be further calculated using geometric relationships, as follows,

$$\Delta z_1 = \Delta s_1 = \Delta\theta(R_c - y_1) \tag{11}$$

$$\Delta z_2 = \Delta s_2 = \Delta\theta(R_c - y_2) \tag{12}$$

The relation of velocities at different points are

$$v_1 = v_m - k y_1 \tag{13}$$

$$v_2 = v_m - k y_2 \tag{14}$$

Combining Eq. (8)–(13), the curvature radius R_c is given by

$$R_c = \frac{v_m}{k} \tag{15}$$

The exit velocities of material at the die orifice as a function of y-coordinate are extracted from numerical simulation as shown in Fig. 8 (c) for different extrusion speed stages. The velocity exhibits a linear increase from the upper side to the lower side of the extrudate, and the velocity gradients, k, are calculated to be 0.0037, 0.0072, 0.0333, and 0.0475 s^{-1} for extrusion speeds of 0.05, 0.1, 0.5, and 1 mm/s, respectively. The intersections of these velocity profiles with the green dashed line, corresponding to $y = 0$, represent v_m, which serves as a representation of the exit velocity of mid points and also the average exit velocity of the profile. For extrusion speeds of 0.05, 0.1, 0.5, and 1 mm/s, the values of v_m are 0.3444, 0.7220, 3.5380, and 7.2413 mm/s respectively.

Combined the results of v_m and k, the curvature radius R_c can be easily calculated according to Eq. (14). Fig. 8(d) shows the values of average exit velocity, velocity gradient and the calculated curvature radius at different extrusion speeds. The average exit velocity exhibits a linear increase with extrusion speed. Conversely, the velocity gradient displays a nonlinear growth pattern with a decreasing rate. The calculated value of R_c, i.e. 93.1 mm at extrusion speed of 0.05 mm/s, 100.3 mm at 0.1 mm/s, 106.2 mm at 0.5 mm/s and 152.4 mm at 1 mm/s, agrees well with the directly measured values in Fig. 8(a). This alignment provides evidence of the correlation between curvature and the uniformity of metal flow, which, in turn, is influenced by the extrusion speed. Therefore, for producing curved profiles with asymmetric cross-section through sideways extrusion, the intrinsic bending phenomena induced by the non-uniform metal flow should be primarily considered before differentiating punch velocities to achieve the target product curvature.

3.3. Analysis of the field variables at different extrusion speeds

Fig. 9 illustrates the flow lines on both the welding plane and the mid flow plane, at three different punch displacements of 0 mm, 6.5 mm and 13 mm, to illustrate the metal flow behaviour. These displacements represent the beginning, midpoint, and end of the first stage of sideways extrusion at 0.05 mm/s, respectively. As shown in Fig. 9(a), the mid flow

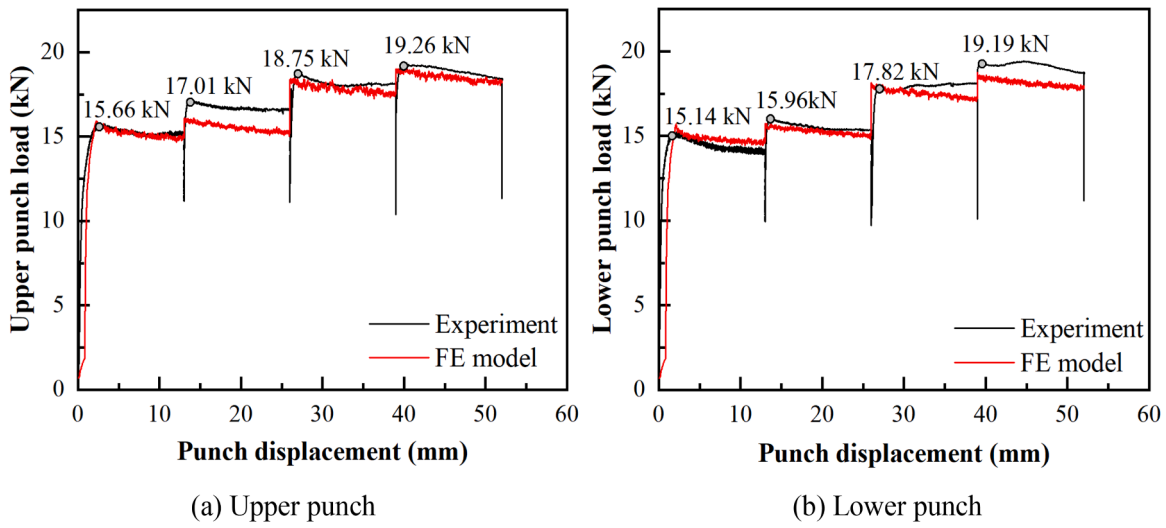

Fig. 7. Comparison of extruson force obtained from experiment (black line) and numerical simulation (red line) for upper and lower punches.

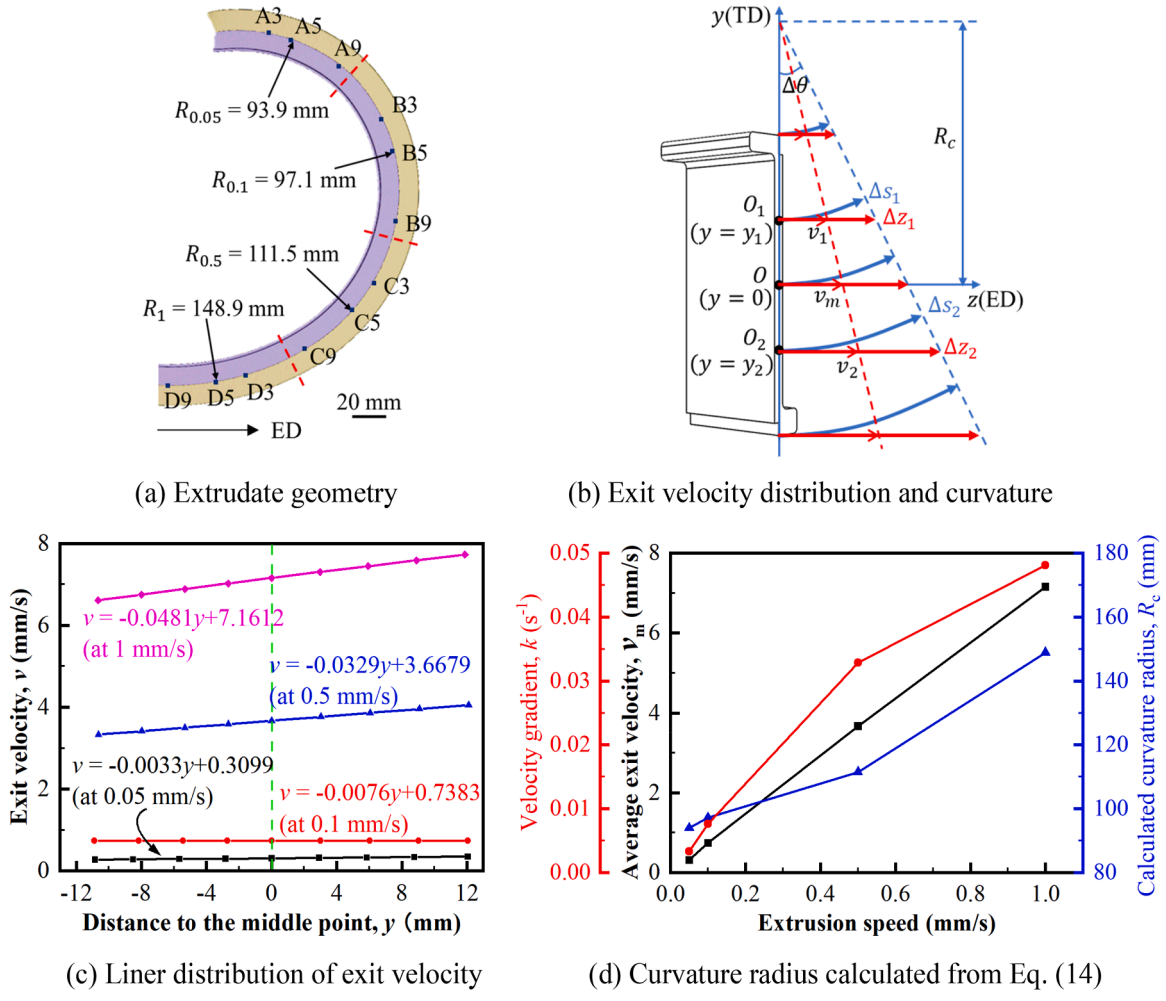

Fig. 8. Analysis of extrudate curvature at different extruson speeds, showing the extruded geometry, velocity distribution and the curvature at the die exit.

plane indicates the ED-TD plane across the billet diameter, while the welding plane signifies the interface between the two billets. Initially, all the mesh grids before extrusion (d = 0 mm) are straight as shown in Fig. 9(b), with those on the welding plane aligning with either the ND or ED and those on the mid flow plane parallel to either the TD or ED. Upon a punch advancement of 6.5 mm, the mesh grids show noticeable distortion in Fig. 9(c). At the punch displacement of 13 mm, the flow lines are distorted more severely as shown in Fig. 9(d). On the welding plane, the flow lines originally parallel to the ED are increasingly compressed towards the ND as they approach the orifice, while those

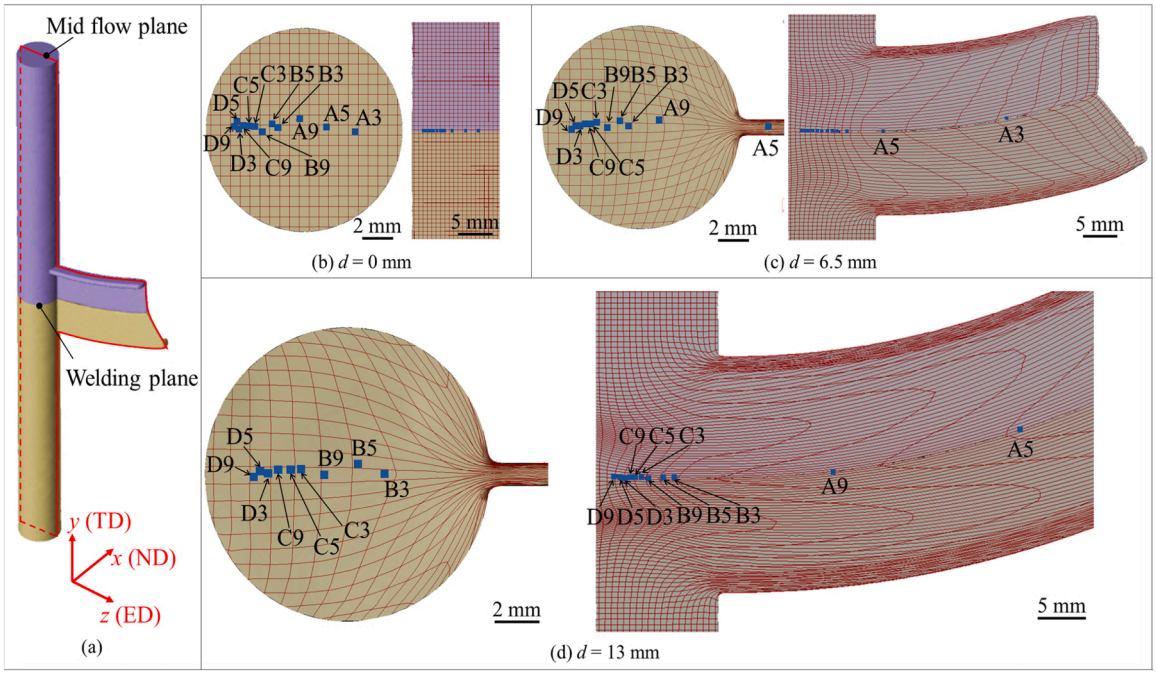

Fig. 9. Mesh grid and tracked points on both the welding plane and mid flow plane at various punch displacements during the first stage of sideways extrusion at 0.05 mm/s.

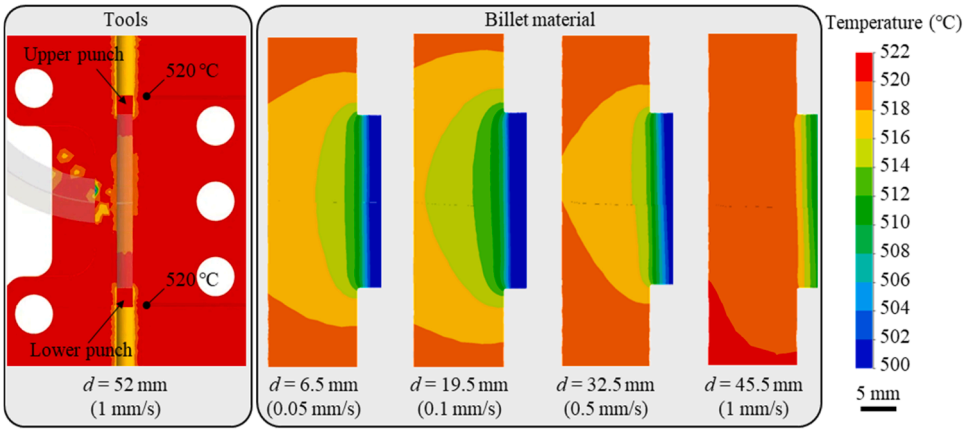

(a) Temperature distribution of tools and workpiece

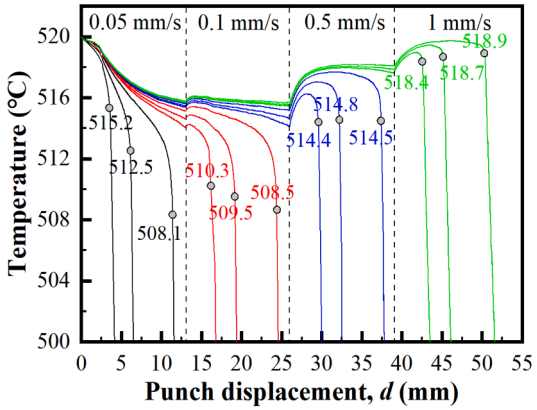

(b) Temperature evolution of tracked points

Fig. 10. Temperature analysis of (a) distribution on the mid flow plane ED-TD at different punch displacements, *d*, with various extrusion speeds, and (b) value evolution of the tracked points in relation to punch displacement where the circles represent the status when the tracked points exit through die orifice. The bottom right corner of (a) shows the scale bar.

initially parallel to the ND contorted, bulging towards the orifice with greater distortion near it. On the mid flow plane, the flow lines initially parallel to the TD transform into curved lines that protrude towards the orifice and then undergo approximately a 90° rotation to enter it, indicating shear deformation. Furthermore, these flow lines from the bottom billet move faster and are more distorted than those from the upper billet due to the higher friction within the upper flange area of the extrudate than that within the bottom flange. This results in the upward curved shape of the final extruded profile.

Twelve points were selected along the intersection line of the welding plane and the mid flow plane of the extrudate as it exits the die orifice at different extrusion progresses. These points are labelled with a combination of letters and numbers to indicate their status at the moment of extrusion from the orifice. The letters A, B, C and D correspond to extrusion speeds of 0.05, 0.1, 0.5 and 1 mm/s, respectively. The numbers 3, 5, and 9 represent the extrusion progress at 30 %, 50 % and 90 % within each speed stage. For example, points A3, A5 and A9 are extruded from the die orifice after 30 %, 50 % and 90 % of extrusion process at the speed of 0.05 mm/s, correlating to punch displacement of 3.9, 6.5 and 11.7 mm, respectively. These points are tracked throughout the whole extrusion process to determine their movement paths. Fig. 9 displays the point positions at the corresponding punch displacements. At $d = 0$ mm, all the points are located on the welding plane between the billets. They are aligned in a straight band, extending in the ED towards the die orifice. At $d = 6.5$ mm (50 % of extrusion at 0.05 mm/s), A3 has already been extruded and A5 is just emerging from the die orifice. At $d = 13$ mm (completion of extrusion at 0.05 mm/s), A3, A5 and A9 have all been extruded, while the remaining points have moved closer to the die orifice but are remain at the interface between the billets.

To evaluate the deformation characteristics across different extrusion speed stages, the distributions of different physical variables on the mid flow plane were captured at different times. This analysis was conducted at four specific times when the punches had advanced by 6.5, 19.5, 32.5, and 45.5 mm, corresponding to reaching 50 % progress of each extrusion at 0.05, 0.1, 0.5, and 1 mm/s, respectively. Additionally, the value evolutions during the extrusion process were plotted for the previously identified twelve points.

Fig. 10 shows the simulation results of temperature of the extrusion die and workpiece. It can be seen from Fig. 10(a) that the temperature at the position of thermocouple is 520 ℃ at the end of extrusion, consistent with the temperature monitored during the extrusion experiment. The temperature distribution on the mid flow plane of the workpiece decreases towards the die orifice and all the temperatures across the entire plane inside the die are within the range from 506 to 522 °C. Notably, the temperature at die orifice is lower than other locations within the die, unlike the typical industrial observation where the workpiece reaches its highest temperature at the orifice. This discrepancy arises from the lab-scale setup, which employs a low extrusion ratio and relatively slow extrusion speeds, resulting in insufficient heat generation at the orifice to offset heat loss to the environment. Fig. 10(b) shows the temperature evolution of the tracked points. For all the points, the temperatures generally decrease with increasing stroke since the points are moving towards the die orifice, with an immediate increase starting at the transition of the extrusion speed from low to high. After exiting

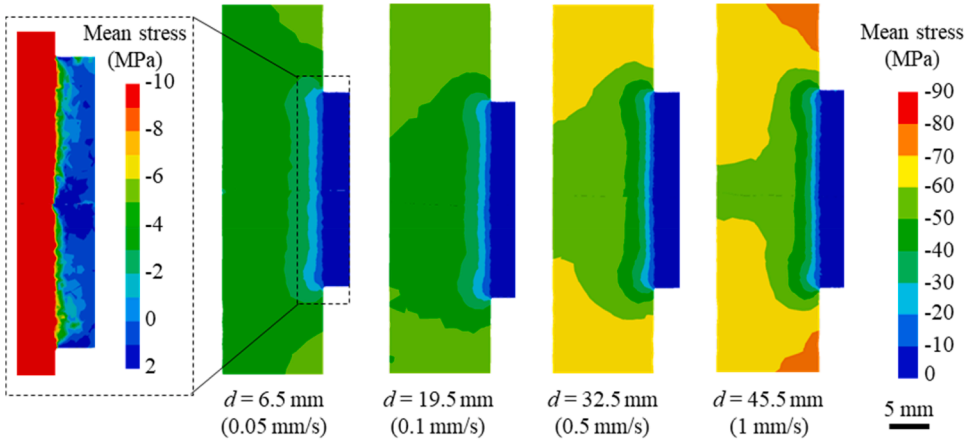

(a) Mean stress distribution

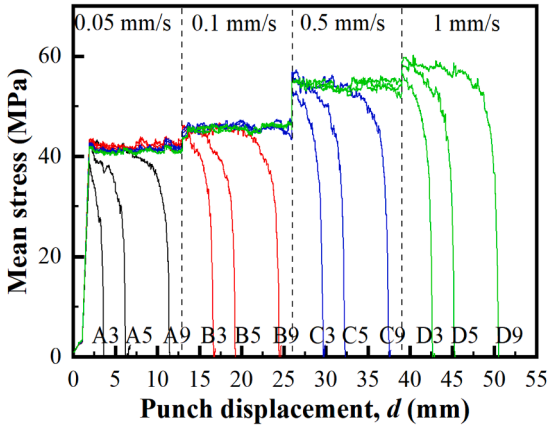

(b) Mean stress evolution of tracked points

Fig. 11. Mean stress analysis of (a) distribution on the mid flow plane ED-TD at different punch displacements, d, with various extrusion speeds, and (b) value evolution of the tracked points in relation to punch displacement.

the die orifice, the temperature drops significantly. The circles in Fig. 10 (b) show the temperature of tracked points at the die orifice, ranging from 508.1 to 518.9 °C due to the combined effect of deformation- and friction- induced heat generation and heat loss to the environment. As the speed increases, the orifice temperature rises from 508.1 to 510.3 °C, 508.5–514.4 °C, and 514.5–518.4 °C, respectively, indicating that higher speeds generate more heat, overcoming environmental losses. At lower speeds (0.05 and 0.1 mm/s), the temperature decreases with punch displacement due to continuous heat loss, whereas at higher speeds (0.5 and 1 mm/s), it increases slightly, suggesting heat generation outweighs heat loss.

Fig. 11(a) shows the distribution of the mean stress, i.e. the average normal stress, on the mid flow plane. The mean stress values at various positions consistently exhibit negative values, signifying material compression during the extrusion process. The absolute magnitude of mean stress is most pronounced at the ends of the billet container, gradually diminishing closer to the die orifice. The close-up of the mid-flow plane at 6.5 mm of punch displacement in Fig. 11(a) reveals that the mean stress at die orifice ranges from −5.49 to 1.68 MPa. The similar phenomenon has been reported in other literature [50,51]. Additionally, it is observed that the absolute mean stress across the entire mid flow plane intensifies with increasing extrusion speed. Fig. 11(b) shows the progression of the absolute mean stress values for the tracked points, commencing from the initiation of the extrusion process until these points exit the die orifice. For all designated points, the absolute mean stress initially surges from a baseline of zero, followed by a gradual increase with a decreasing growth rate, culminating in a plateau. Subsequently, a decrease ensues as the material flows through die orifice. A noticeable abrupt increase in stress occurred during the transition from lower extrusion speeds to higher ones.

The mid flow plane exhibits low effective stress levels at the billet ends, as depicted in Fig. 12(a). This stress gradually increases towards the middle region and peaked along the die orifice. With the advancement of the extrusion, the overall distribution of effective stress increases. Fig. 12(b) depicts the evolution of effective stress for all monitored points, showing a gradual increase, followed by a marked surge as they pass through the die orifice, and a sharp decline thereafter. The maximum effective stress remains consistent for points extruded at the same extrusion speed as shown in Fig. 12(b). Notably, an abrupt increase is observed when transitioning from low to high extrusion speeds, with the maximum effective stress intensifying as the extrusion speeds rise. Therefore, it can be inferred that the effective stress at the die orifice is significantly influenced by the speed of extrusion, while its relationship to punch displacement is comparatively less pronounced.

Fig. 13(a) shows the strain rate field on the mid flow plane at various stages of punch advancement. The highest strain rate is observed at the die orifice, with lower values in other areas away from the orifice. As the extrusion speed increases, the strain rate near the die orifice rises

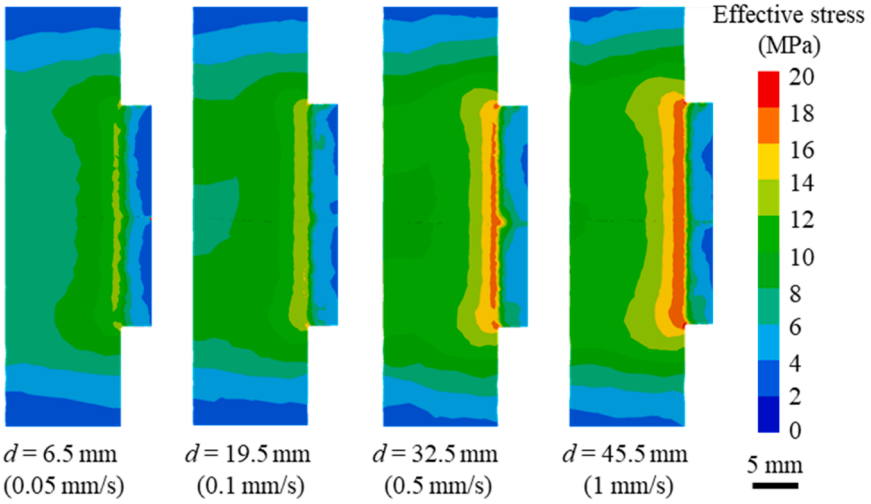

(a) Effective stress distribution

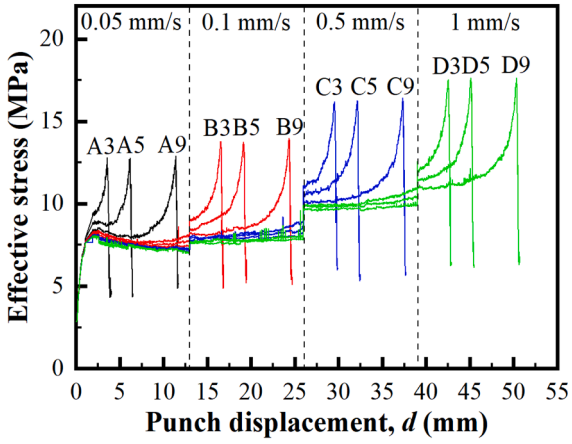

(b) Effective stress evolution of tracked points

Fig. 12. Effective stress analysis of (a) distribution on the mid flow plane ED-TD at different punch displacements, *d*, with various extrusion speeds, and (b) value evolution of the tracked points in relation to punch displacement.

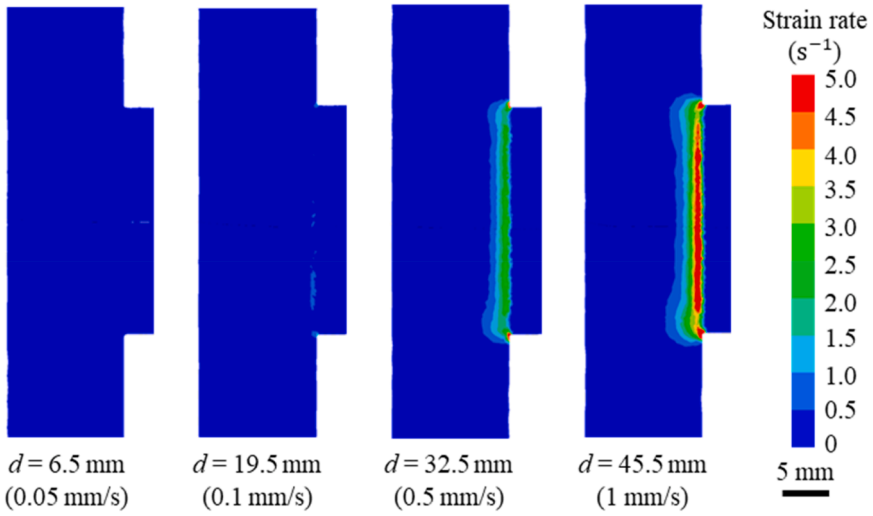

(a) Strain rate distribution

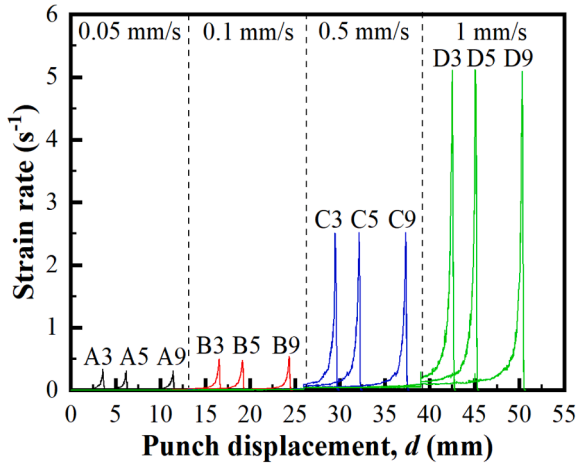

(b) Strain rate evolution of tracked points

Fig. 13. Strain rate analysis of (a) distribution on the mid flow plane ED-TD at different punch displacements, *d*, with various extrusion speeds, and (b) value evolution of the tracked points in relation to punch displacement.

dramatically while other regions continue to exhibit low strain rate. This observation is consistently reflected in Fig. 13(b), where the strain rate for the tracked points experiences a significant increase as they pass through the die orifice, followed by a decline to zero once they emerge. The maximum strain rate remains consistent at the same extrusion speed but increases with higher extrusion speeds. This pattern suggests that while the strain rate field is highly sensitive to extrusion speed, it is less influenced by the progression of extrusion process.

Fig. 14(a) presents the effective strain distributions on the mid flow plane at different punch displacements. A significant portion of plastic deformation happens in the proximity to the die orifice, with the highest effective strain concentrated within the welding zone of the extrudate. This is mainly attributed to the frictional interactions between different billets during the extrusion process. As the extrusion speed increases, the effective strain also becomes higher. The evolutions of effective strain for the tracked points are plotted in Fig. 14(b), showcasing a progressive increase that culminates in the maximum value after the material exits the die orifice. No notable abrupt changes were detected across various extrusion speeds, indicating the limited influence of extrusion speed on effective strain during sideways extrusion. Moreover, upon comparing the final effective strain of different points, it can be deduced that materials extruded at a later stage acquire a greater effective strain than those extruded earlier. Fig. 14(c) further accentuates that the ultimate effective strain exhibits a proportional increase relative to punch displacement.

Fig. 15 presents the contours of strain components ε_{yy}, ε_{zz} and τ_{yz} on the mid flow plane at the punch displacement of 32.5 mm. The visualisation highlights the compression occurring along the TD direction, coupled with elongation along the ED direction. This distinctive strain pattern holds substantial implications for the ensuing microstructural evolution, a discussion that will be expounded upon in Section 4.4.

3.4. Welding quality evaluation of extrudate

3.4.1. Simulated welding quality (J index analysis)

According to Eq. (2), the welding quality is greatly influenced by physical variables such as mean stress, effective stress, and strain rate. Fig. 16(a–c) illustrates the distribution of these variables on the welding plane at a punch displacement of 32.5 mm. Fig. 16(a) shows that the absolute mean stress gradually diminishes as one moves closer to the die orifice, while Fig. 16(b) indicates an increase in effective stress towards the orifice. Fig. 16(c) reveals the strain rate to be the highest near the die orifice, tapering off with distance from the orifice. Utilising this data, the subroutine presented in Fig. 4(a) was employed to simulate the *J* index distribution on the welding plane throughout the sideways extrusion process. Fig. 16(d) illustrates the *J* index distributions at four different

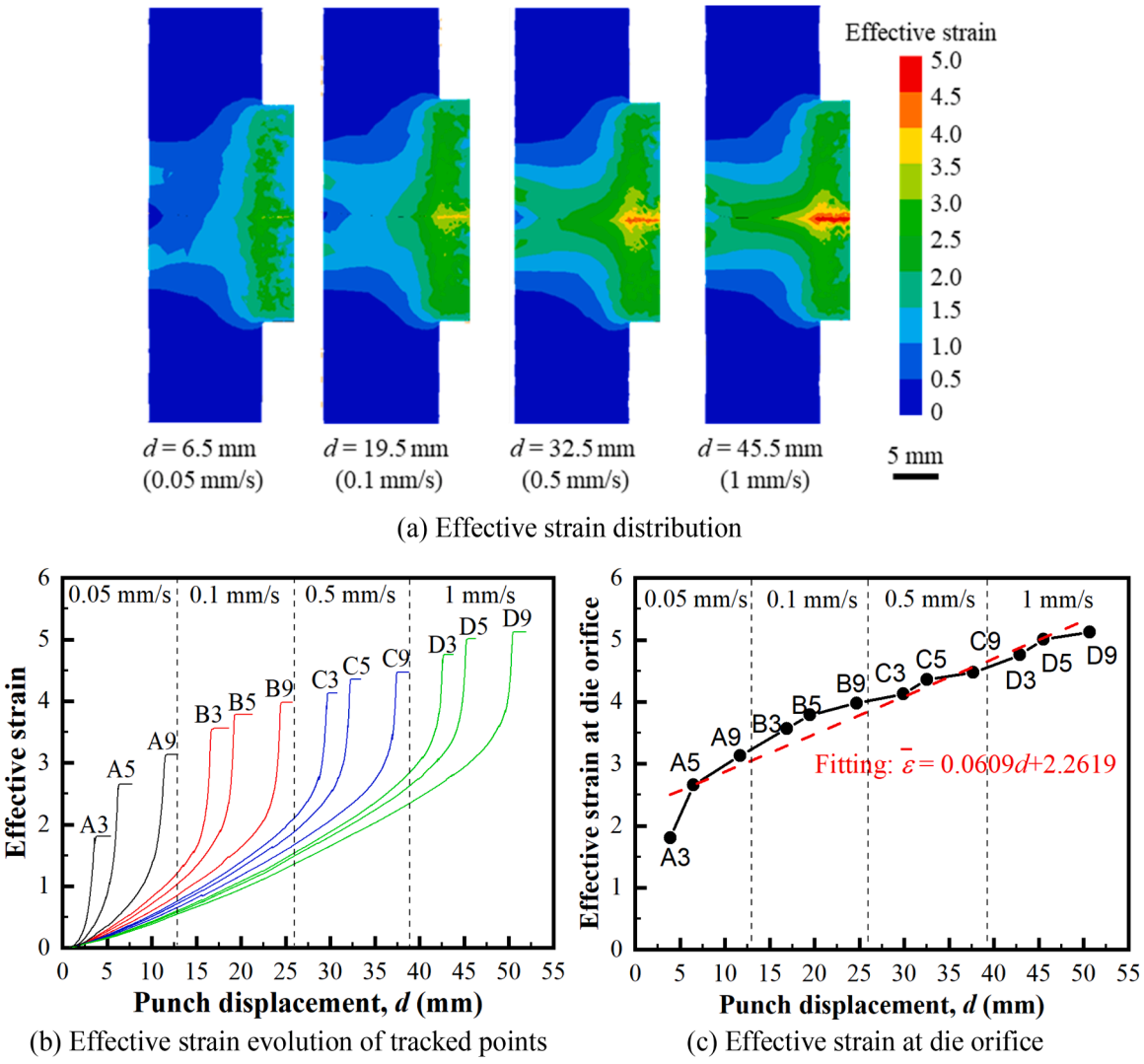

Fig. 14. Effective strain analysis of (a) distribution on the mid flow plane ED-TD at different punch displacements, *d*, with various extrusion speeds, (b) value evolution of the tracked points in relation to punch displacement, and (c) the relation of punch displacement when the tracked points exit the die orifice.

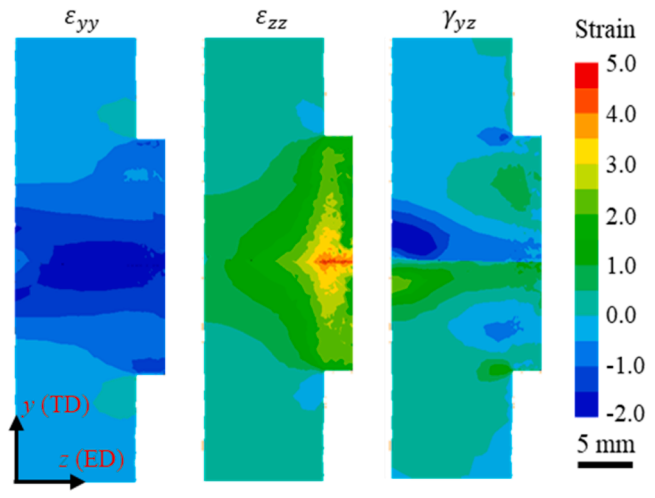

Fig. 15. Distribution of strain component along TD and ED direction, respectively, on the mid flow plane ED-TD at the punch displacement of $d = 32.5$ mm.

punch displacements, corresponding to the 50 % completion of the extrusion at various extrusion speed stages. The *J* index escalates near the die orifice and, as the extrusion progresses, there is a gradual overall increase in the *J* index, demonstrating the improvement of welding quality. Additionally, the welding quality of the extrudate is enhanced along the edges compared to its centre. This is attributed to the higher strain rate and absolute mean stress applied to the marginal area of the extrudate. Fig. 16(e) further illustrates the *J* indices obtained by the tracked points after exiting the die orifice, plotted as a function of punch displacement. Points extruded later exhibit higher *J* indices compared to those extruded earlier, signifying a gradual enhancement in welding quality during the extrusion process.

3.4.2. *Optical microscopy observations of welds*

Fig. 17 presents the optical microscopy images of the mid flow plane of the extrudate These images were captured at the middle part of the profile section extruded at various speed of 0.05, 0.1, 0.5 and 1 mm/s as shown in Fig. 5, corresponding to points A5, B5, C5 and D5 in the numerical simulation, respectively. For the sample extruded at 0.05 mm/s (Fig. 17(a)), a distinct and continuous seam is clearly visible along the welding interface. As the extrusion speed increases to 0.1 mm/s (Fig. 17 (b)), the welding line becomes less distinct and exhibits a discontinuous nature. At 0.5 mm/s (Fig. 17(c)) and 1 mm/s (Fig. 17(d)), the entire

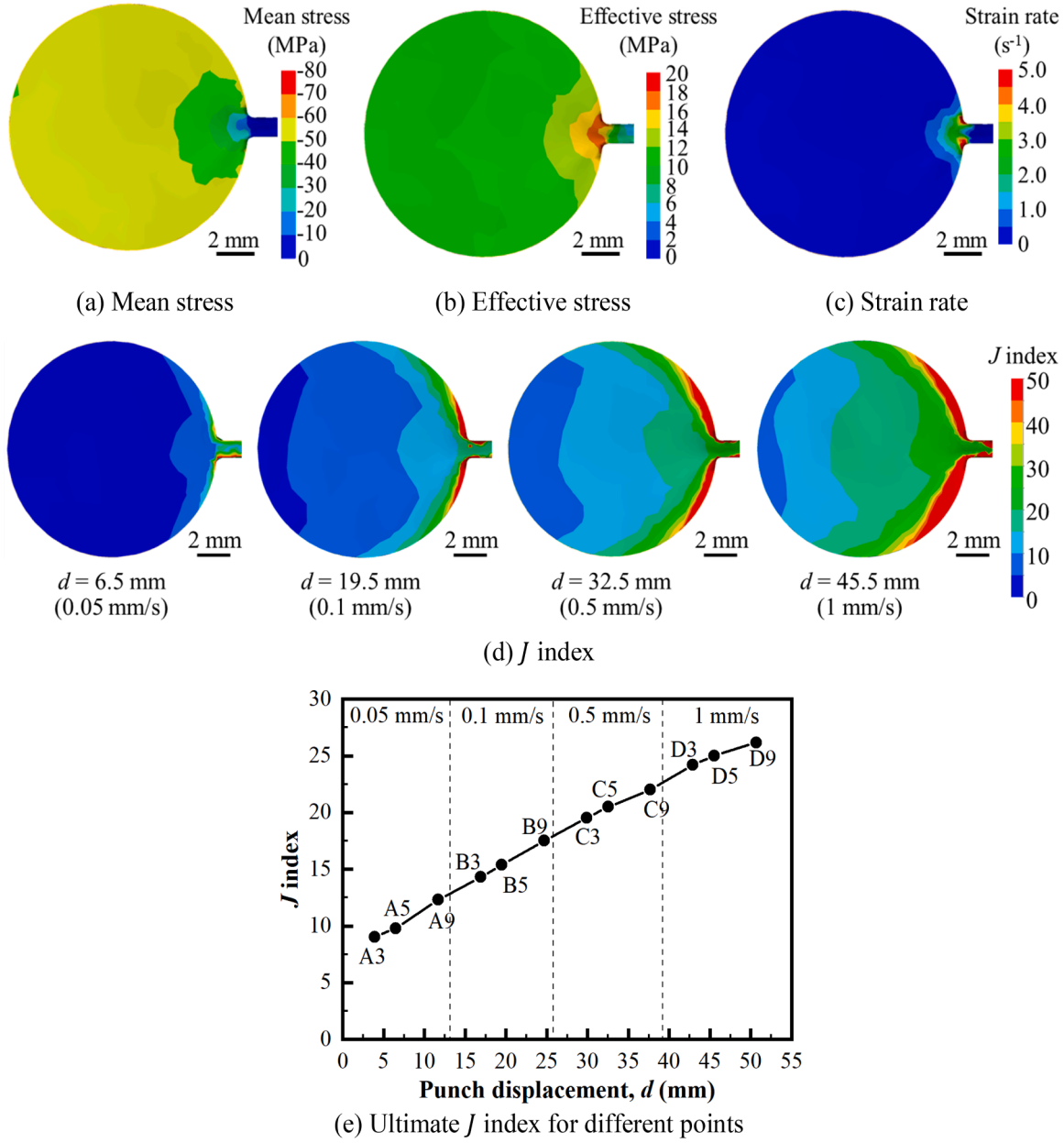

Fig. 16. Variable fields on the welding plane ED-ND for (a) mean stress, (b) effective stress, and (c) strain rate at the punch displacements of $d = 32.5$ mm; (d) J index at different punch displacements with various extrusion speeds; and (e) ultimate J index of different tracked points as a function of punch displacement.

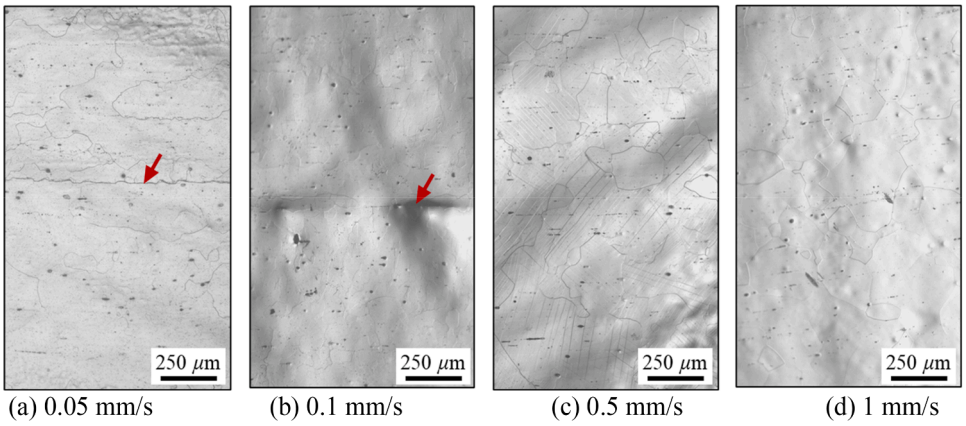

Fig. 17. Optical micrographs of the mid flow plane of the material extruded at varioius speeds, where red arrows indicate the weld seams.

welding line disappears. The progressive reduction in the visibility of the welding line during the extrusion process suggests an enhancement in welding quality as the extrusion progresses. The key factors influencing interface welding include the ratio of welding pressure (absolute mean stress) to effective stress ($|\sigma_m|/\overline{\sigma}$) temperature, strain rate, and welding time, based on two primary mechanisms. The first mechanism involves plastic deformation-induced void closure, where a higher strain level - represented by the integral of the product of strain rate and welding time ($\int \dot{\varepsilon} dt$) - promotes void closure. Additionally, a higher $|\sigma_m|/\overline{\sigma}$, which indicates relatively high welding pressure and low resistance to deformation, helps shrink voids and improves weld quality. The second mechanism is atomic diffusion-induced void closure, which increases the activity of atoms with higher temperatures. In this study, the effective strain level rises as extrusion proceeds as shown in Fig. 14, aiding in welding. Both welding pressure and effective stress increase as shown in Fig. 11 and Fig. 12, complicating the direct assessment of their ratio's evolution. Billet material temperature fluctuates as shown in Fig. 10, making a direct evaluation of welding quality challenging. The J index from the simulation effectively reflects the combined impact of stress state, temperature, strain rate, and welding time on welding quality, showing a trend of improvement (Fig. 16) that aligns well with OM observations.

3.5. Microstructural analysis of extrudate

3.5.1. Simulated recrystallisation (DRX) fraction

Based on the strain field and strain rate field as depicted in Fig. 14 and Fig. 13, and utilising Eq. (5), the DRX fraction X_{DRX} was simulated and presented in Fig. 18. Fig. 18(a) displays the distribution of X_{DRX} on the mid flow planes at various punch displacements, each corresponding to the halfway point of extrusion at different speeds. Notably, for each speed, X_{DRX} progressively increases towards the die orifice, with a distribution pattern similar to that for effective strain in Fig. 14(a). There is an overall increase in X_{DRX} as the extrusion advances and the extrusion speed increases. Fig. 18(b) illustrates the ultimate values of X_{DRX} at tracked points after exiting the die orifice, i.e. the final DRX fraction in the extruded profile. These values exhibit a continuous increase with punch displacement, signifying that the materials extruded later attained a higher degree of DRX than those extruded earlier. Despite the extrusion rate increasing with higher extrusion speeds during the sideways extrusion disfavours the DRX occurrence, the gradually increased X_{DRX}demonstrates that the effective strain predominantly influences DRX in this study. This increase in DRX fraction will undergo further corroboration through upcoming microstructural tests.

3.5.2. Characteristics of grain boundaries and dislocations

Fig. 19 presented the EBSD inverse pole figure (IPF) and boundary maps of selected zones extruded at various speeds. In the IPF images,

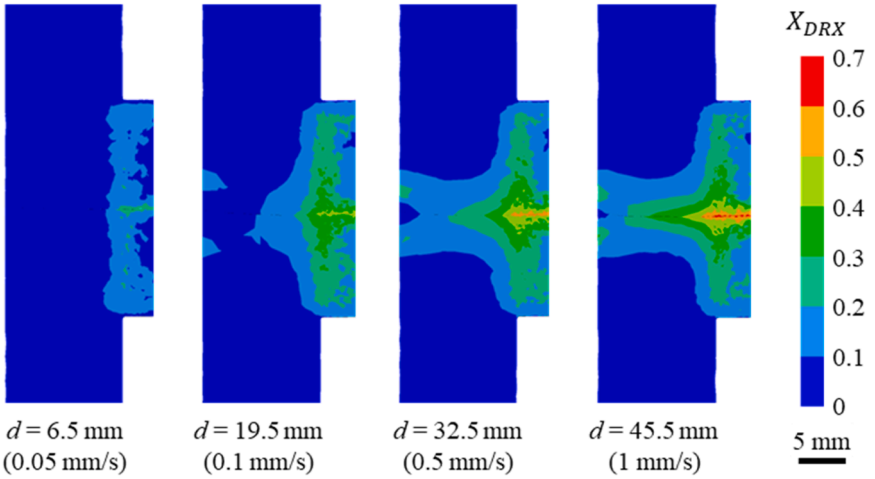

(a) X_{DRX} on the mid flow plane

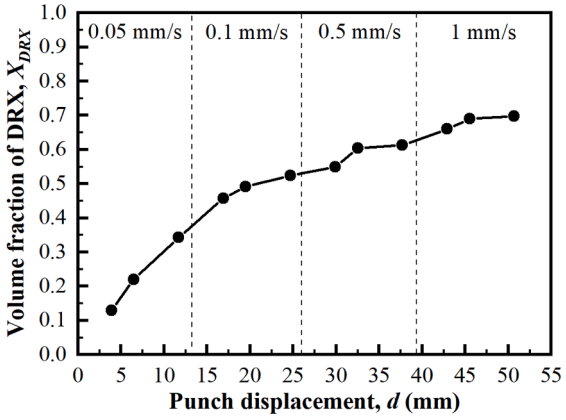

(b) X_{DRX} for different points after extrusion

Fig. 18. Simulated DRX fraction, X_{DRX}, on the mid flow plane ED-TD at different punch displacements, d, with various extrusion speeds and its final values after extrusion for different tracked points as a function of punch displacement.

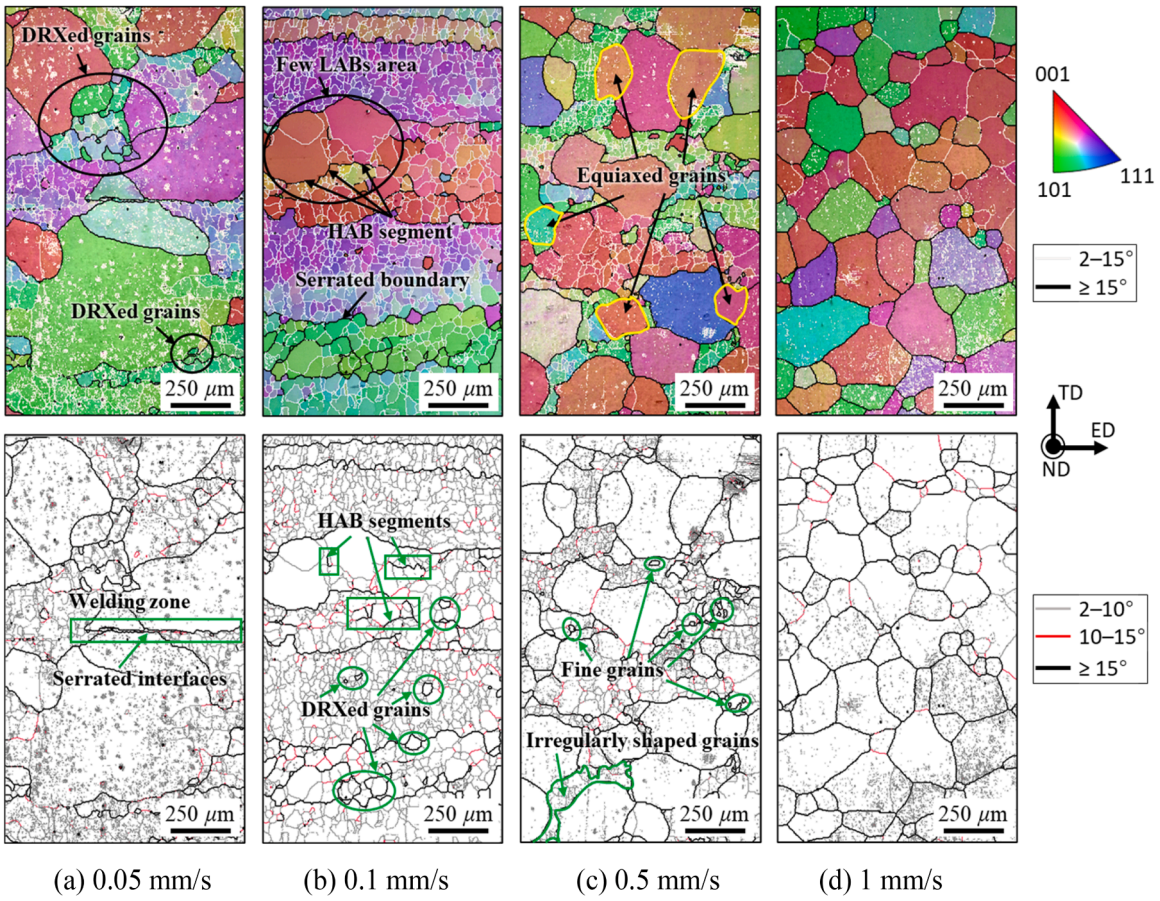

Fig. 19. EBSD inverse pole figure maps and low angle and high angle grain boundaries at selected zones for different extrusion speeds.

black lines represent high angle boundaries (HABs, with a misorientation angle $\theta \geq 15°$) and light grey lines represent LABs (with a misorientation angle of $2° \leq \theta < 15°$). Within the boundary maps, LABs are further divided into two misorientation angle ranges of $2° \leq \theta < 10°$ (grey lines) and $10° \leq \theta < 15°$ (red lines). The initial billet exhibits an average grain size of approximately 3 mm, and it possesses few substructures. After the sideways extrusion, as shown in Fig. 19(a), more LABs are formed in the profile extruded at 0.05 mm/s. Additionally, some fine grains ranging from 13—52 μm are formed, as indicated within the black circle in the IPF map. Analysing the boundary map in Fig. 19(a), it is apparent that most LABs around the fine grains possess relatively high misorientation angles, typically in the range of 10—15°. This indicates that the primary mechanism responsible for the formation of these new grains is continuous dynamic recrystallisation (CDRX). Furthermore, two serrated lines with a small gap can be observed along the welding interface within the green box in the boundary map. This observation suggests that during the extrusion at 0.05 mm/s, some surfaces between the two billets were unable to make complete bonding due to relatively low welding pressure as characterised in Fig. 11(b).

Fig. 19(b) shows the microstructures of the profile extruded at 0.1 mm/s. These grains appear severely elongated, and the grain boundaries exhibit a serrated pattern, indicative of the higher levels of strain experienced compared to the material extruded at 0.05 mm/s. This microstructural observation aligns with the simulation results presented in Fig. 15, which indicates tension along ED (z-coordinate) and compression along TD (y-coordinate). LABs are uniformly distributed within the elongated grains, giving rise to a significant number of equiaxed subgrains. This phenomenon is attributed to the dynamic recovery mechanism, where dislocations accumulate to form LABs through processes such as climb or cross-slip. Additionally, within the black circle in Fig. 19(b), an area is identified with few LABs. This may be linked to the CDRX mechanism and the presence of HAB segments, as indicated by the arrows in the IPF map. Compared to Fig. 19(a), there is a higher prevalence of LABs with misorientation angles of 10—15° and new grains formed during the extrusion at 0.1 mm/s. This illustrates that as the extrusion progresses with higher levels of strain and strain rate, the extent of dynamic recrystallisation (DRX) increases, which aligns well with the predicted increase in DRX fraction, X_{DRX}, in Fig. 18(b). Many HAB segments are also observed within the large grains as indicated by green boxes in the boundary map, further confirming that CDRX is the primary mechanism driving the generation of new grains. Unlike the observation in Fig. 19(a), there is no clear evidence of a boundary gap along the welding interface and interface appears wavy due to boundary migration, indicating an improved welding quality.

In Fig. 19(c), the microstructure of the profile extruded at 0.5 mm/s exhibits three discernible characteristics: equiaxed grains of approximately 100–300 μm in size, displaying few substructures as outlined with yellow edges in the IPF map; irregularly shaped grains featuring a higher density of LABs as outlined with green edges in the boundary map; and fine grains formed either along grain boundaries or within the irregularly shaped grains as indicated by green circles and arrows in the boundary map. These findings collectively suggest a comparatively higher degree of recrystallisation during the 0.5 mm/s extrusion compared to preceding processes at lower speeds. Fine grains emerge through CDRX, and certain recrystallised grains grow into relatively larger grains. Notably, like the corresponding OM result in Fig. 17(c), the EBSD map also does not distinctly reveal a welding line for the profile extruded at 0.5 mm/s.

At the highest extrusion speed of 1 mm/s, the microstructure exhibits equiaxed grains ranging in size from approximately 13 μm to 300 μm, distributed uniformly without intensive LABs, as demonstrated in Fig. 19(d). The boundary map reveals the presence of LABs with

misorientation angles of 10—15°, represented by red lines intersecting the grains and forming equiaxed subgrains, signifying an incomplete CDRX process. Combining these findings with the simulation results from Fig. 18, it can be deduced that as extrusion progresses from low to high speeds, where both strain and strain rate increase, new grains are increasingly generated through CDRX. Simultaneously, the welding interface experiences further improved bonding due to higher strain-induced interface grain boundary (IGB) migration, ultimately leading to its disappearance as a result of the new grain formation. The evolution of the weld seams and the improvement of welding quality shown in Fig. 19 correspond well to the increase in *J* index in Fig. 16(e).

Fig. 20 shows the misorientation angle distribution at the selected zones for different extrusion speeds. The fractions of the misorientation angles falling within the ranges of 2—10°, 10—15° and ≥ 15° are calculated for all the selected zones. At the beginning of the sideways extrusion, i.e. at 0.05 mm/s (Fig. 20(a)), the LABs have been significantly increased due to the increasing plastic deformation shown in Fig. 14. For the extrusion at 0.1 mm/s (Fig. 20(b)), the fraction of LABs of 2—10° decreases while that of 10—15° increases compared to the extrusion at 0.05 mm/s. HABs also increase slightly. This demonstrates that the misorientation angle of LABs gradually increases and more LABs transform into HABs due to the increase of plastic strain, indicating the occurrence of CDRX. As the extrusion speed increases to 0.5 mm/s in Fig. 20(c), the fraction of LABs with misorientation in the range of 2—3° significantly increase from 20 % at 0.1 mm/s to 35 % at 0.5 mm/s. This can be attributed to the influence of strain rate, where the higher strain rate leaves less time for dynamic recovery and hence hinder the movement of dislocation and the increase in misorientation of LABs [52]. Despite that, it is observed that more HABs are furtherly formed which is related to the higher level of CDRX induced by the increasing strain. Fig. 20(d) shows that the fraction of LABs of 2—3° increases further due to the restrained recovery by the high strain rate. On the other hand, induced by the increasing strain, more LABs have transformed into HABs. This results in an increased fraction of HABs in the extruded profile at 1 mm/s, indicating a more pronounced degree of CDRX occurring.

Fig. 21 presents the geometrically necessary dislocation (GND) density maps for different extrusion speeds. During the sideways extrusion process, more dislocations are generated by the continuous plastic deformation. Meanwhile, these generated dislocations can be entangled to form LABs or annihilated during dynamic recovery (DRV) and CDRX. The combined mechanisms result in dynamic changes in GND density, progressing from 0.28×10^{14} /m² at 0.05 mm/s, to 0.16×10^{14} /m² at 0.1 mm/s, 0.27×10^{14} /m² at 0.5 mm/s, and 0.26×10^{14} /m² at 1 mm/s. These variations can be analysed in light of simulation results for material temperature (Fig. 10), effective strain (Fig. 14), and CDRX fraction (Fig. 18). At 0.5 mm/s, i.e. 0–260 s of extrusion, the relatively low temperature and strain result in a low CDRX level. This stage yields material with numerous strain-induced GNDs, as seen in Fig. 21(a). At the 0.1 mm/s stage (260–390 s), increased deformation time, temperature, and effective strain lead to higher CDRX, transforming GNDs into LABs as evidenced in Fig. 19(b), reducing GND density (Fig. 21(b)). During the subsequent 0.5 mm/s stage (390–416 s), higher temperature and strain further enhance CDRX, while the

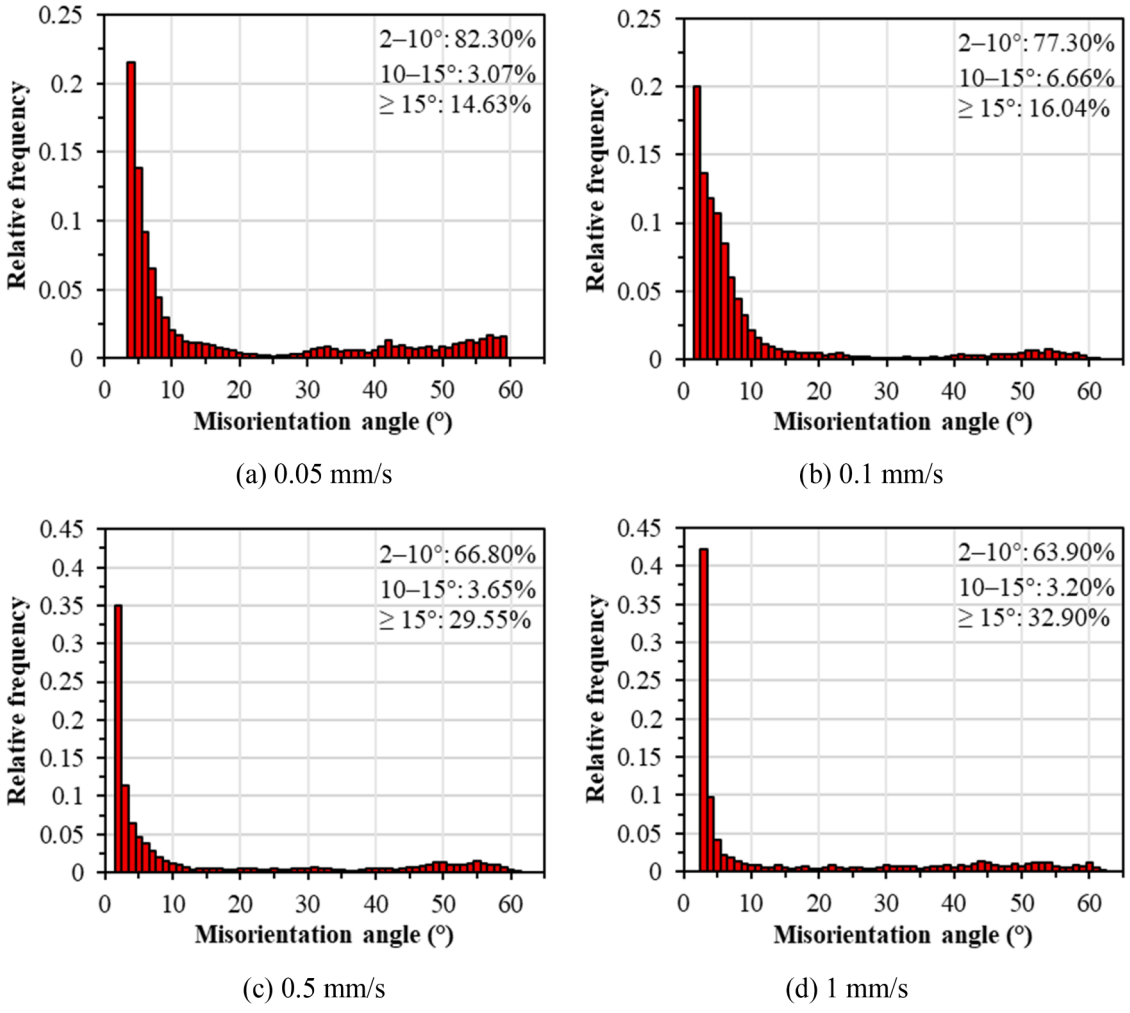

Fig. 20. Misorientaton angle disribution at selected zones from profile extruded at different speeds, where red arrows indicate the weld seams.

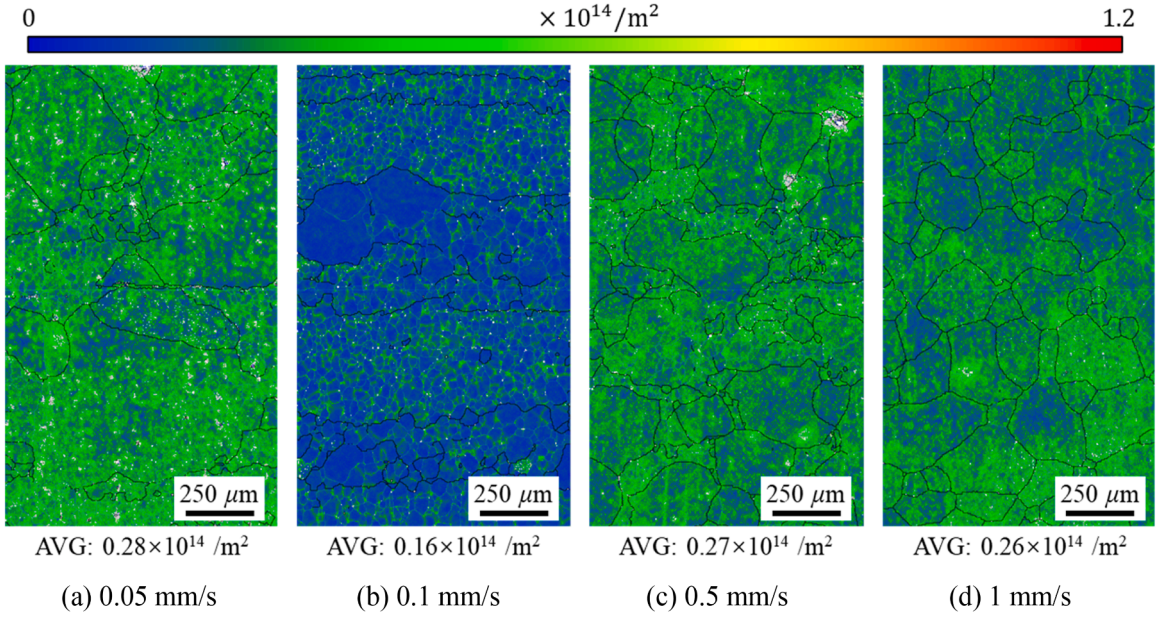

Fig. 21. Geometrically necessary dislocation (GND) density maps at selected zones from profile extruded at different speeds.

continued strain generates additional GNDs, increasing GND density once more (Fig. 21(c)). Finally, at 1 mm/s (416–429 s), the CDRX fraction peaks at 70 %, reducing existing GNDs even as increased strain generates new ones, causing a slight GND density decrease (Fig. 21(d)).

Based on the analysis of Figs. 19–21, the characteristics of microstructural evolution during sideways extrusion become evident. Three concurrent mechanisms influence the microstructure concurrently: work hardening, DRV (softening) and CDRX (softening) during the extrusion process. As extrusion progresses, the formation of more equiaxed grains and the transformation of LABs to HABs suggest a continuous increase in the CDRX fraction. Additionally, the evolution of GND density is more complex and does not follow a monotonic trend. The increasing plastic deformation during extrusion promotes the generation of dislocations, while the simultaneous occurrence of DRV and CDRX leads to the annihilation of dislocations. The interplay and relative activities of these three mechanisms, greatly influenced by the levels of strain and strain rate, ultimately determine the final GND density.

3.6. *Mechanical properties of the extrudate*

Fig. 22(a) shows stress-strain curves obtained from the tensile tests and Fig. 22(b) shows the corresponding data of 0.2 % proof stress (yield strength), ultimate tensile strength (UTS) and elongation to fracture. Compared to the billet, the extruded materials at different speeds all obtained a higher yield strength, higher UTS and lower elongation to fracture. Since the weld formed by the two billets during sideways extrusion locates in the middle region of the tensile testing specimens, the yield strength, UTS and elongation properties can be influenced by both the welding quality and the matrix material property. It has been shown by other researchers that ductility of material can be deteriorated more sensitively by poor welding quality than the strengths [53]. This aligns well with the elongation values obtained in this study, i.e. the elongation to fracture of the extrudate gradually increases with the improving welding quality as the extrusion progresses and the extrusion speed increases. On the other hand, the yield strength and UTS results are prone to the effect of matrix microstructure. Combined with Fig. 21, the material with more dislocations has higher yield strength and UTS, which corresponds to the strain hardening mechanism.

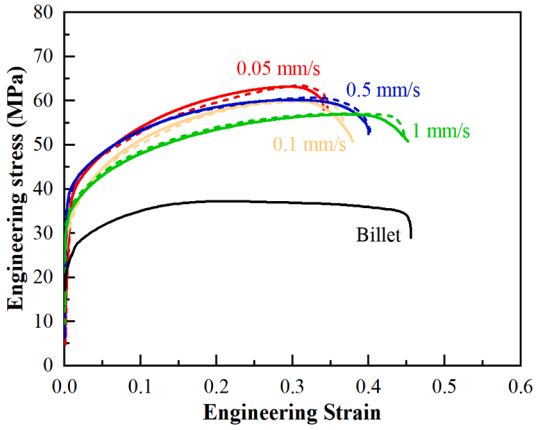

(a) Stress-strain curves

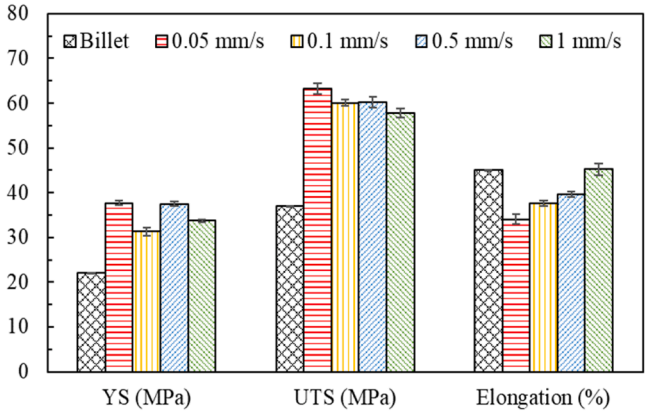

(b) Bar chart of yield strength, UTS and elongation

Fig. 22. Mechanical properties of the billet and extruded profile at differet speeds.

4. Conclusions

In this study, aluminium profiles with a Z-shape cross-section were produced through a novel sideways extrusion method involving discontinuously increased extrusion speeds (0.05, 0.1, 0.5 and 1 mm/s). The weld quality, and the microstructural and mechanical properties of the profile were examined experimentally. Numerical simulation incorporating two user-defined subroutines was conducted to quantitatively analyse the metal flow behaviour, physical variable distributions, welding quality, and recrystallisation fraction. The combination of experimental and numerical results provided a comprehensive understanding of the sideways extrusion process for asymmetric profiles. The following conclusions are drawn:

(1) Extrudate exhibits bending due to non-uniform flow during sideways extrusion. This bending results in distinct curvature radii along its length corresponding to different extrusion speeds. The curvature radius was found equal to the ratio of the average exit velocity to the velocity gradient across the cross-section. As the extrusion speed increases, the average exit velocity proportionally increases, while the rate of increase of the velocity gradient is reduced, leading to the increase in curvature radius.
(2) The weld quality in the extruded profile is continuously improved with the progress of extrusion and the increase of extrusion speed. At the front of the extruded profile, with an extrusion speed of 0.05 mm/s, there is a visible continuous weld seam along the bonding surface. As the extrusion proceeds and the speed increases to 0.1 mm/s, this weld seam becomes less distinct and ultimately becomes imperceptible at speeds of 0.5 and 1 mm/s. These observations correspond well with the simulation results, where the J index (a measure of welding quality) increases with the extrusion process, indicating that sideways extrusion can produce profiles with good weld quality except for the front part. In addition, innovatively integrating J criterion into simulation process provides a straightforward method for quantitatively evaluating the welding plane, from within the extrusion tool to the orifice.
(3) Continuous dynamic recrystallisation (CDRX) occurs with its activity increasing as the extrusion proceeds due to the increasing material effective strain. Experimentally, this is demonstrated by the continuous transformation of LABs to HABs. Numerically, it is supported by the rising fraction of DRX during the extrusion process. On the other hand, the geometrically necessary dislocation (GND) density exhibits a non-monotonic evolution due to the combined effect of work hardening, recovery and CDRX.
(4) The material after sideways extrusion exhibits a notable increase in yield strength and ultimate tensile strength (UTS), coupled with a decrease in elongation to failure compared to the original billet. The mechanical properties vary at different positions along the extrudate. Notably, the elongation is most sensitive to welding quality, exhibiting greater values in materials extruded at later stage compared to those extruded earlier. On the other hand, yield strength and UTS correspond closely with the dislocation density within the matrix material.

CRediT authorship contribution statement

Jiaxin Lv: Investigation, Visualization, Software, Data curation, Writing – original draft. **Xiaochen Lu:** Investigation, Resources. **Junquan Yu:** Methodology, Investigation, Writing – Reviewing and Editing. **Zhusheng Shi:** Conceptualization, Supervision, Writing – Reviewing and Editing. **Jianguo Lin:** Conceptualization, Funding acquisition, Supervision.

Declaration of Competing Interest

The authors declare that they have no known competing financial interests or personal relationships that could have appeared to influence the work reported in this paper.

Acknowledgements

This work was supported by the UK Engineering and Physical Sciences Research Council (EPSRC) (grant No: EP/S019111/1; UK FIRES: Locating Resource Efficiency at the heart of Future Industrial Strategy). Junquan Yu would like to acknowledge the financial supports from the National Natural Science Foundation of China (52205388).

Data Availability

Data will be made available on request.

References

[1] Hashimoto, N., 2017. Application of Aluminum extrusions to automotive parts. KOBELCO Technol. Rev. 35, 69–75.
[2] The 17 Goals of Sustainable Development. ⟨https://sdgs.un.org/goals⟩; [Accessed 10 August 2023].
[3] Lv, J., Yu, J., Shi, Z., Li, W., Lin, J., 2023. Feasibility study of a novel multi-container extrusion method for manufacturing wide aluminium profiles with low force. J. Manuf. Process. 85, 584–593.
[4] Liu, Z., Li, L., Yi, J., Wang, G., 2019. Entrance shape design of spread extrusion die for large-scale aluminum panel. Int. J. Adv. Manuf. Technol. 101, 1725–1740.
[5] Wang, D., Zhang, C., Wang, C., Zhao, G., Chen, L., Sun, W., 2018. Application and analysis of spread die and flat container in the extrusion of a large-size, hollow, and flat-wide aluminum alloy profile. Int. J. Adv. Manuf. Technol. 94, 4247–4263.
[6] Hu, J., Zhang, W., Fu, D., Teng, J., Zhang, H., 2019. Improvement of the mechanical properties of Al–Mg–Si alloys with nano-scale precipitates after repetitive continuous extrusion forming and T8 tempering. J. Mater. Res. Technol. 8, 5950–5960.
[7] Tang, W., Reynolds, A.P., 2010. Production of wire via friction extrusion of aluminum alloy machining chips. J. Mater. Process. Technol. 210, 2231–2237.
[8] Taysom, B.S., Overman, N., Olszta, M., Reza-E-Rabby, M., Skszek, T., DiCiano, M., Whalen, S., 2021. Shear assisted processing and extrusion of enhanced strength aluminum alloy tubing. Int. J. Mach. Tools Manuf. 169, 103798.
[9] Müller, K.B., 2006. Bending of extruded profiles during extrusion process. Int. J. Mach. Tools Manuf. 46, 1238–1242.
[10] Zhou, W., Lin, J., Dean, T.A., Wang, L., 2018. Feasibility studies of a novel extrusion process for curved profiles: experimentation and modelling. Int. J. Mach. Tools Manuf. 126, 27–43.
[11] Zhou, W., Lin, J., Dean, T.A., Wang, L., 2018. Analysis and modelling of a novel process for extruding curved metal alloy profiles. Int. J. Mech. Sci. 138-139, 524–536.
[12] Zhou, W., Yu, J., Lu, X., Lin, J., Dean, T.A., 2021. A comparative study on deformation mechanisms, microstructures and mechanical properties of wide thin-ribbed sections formed by sideways and forward extrusion. Int. J. Mach. Tools Manuf. 168, 103771.
[13] Liu, J., 1999. Aluminum Extrusion Die Design, Manufacture, Use and Maintenance. Metallurgical Industry Press of China.
[14] Mayavaram, R., Sajja, U., Secli, C., Niranjan, S., 2013. Optimization of bearing lengths in aluminum extrusion dies. Procedia CIRP 12, 276–281.
[15] Wu, X., Zhao, G., Luan, Y., Ma, X., 2006. Numerical simulation and die structure optimization of an aluminum rectangular hollow pipe extrusion process. Mater. Sci. Eng. A 435, 266–274.
[16] Llorca-Schenk, J., Sentana-Gadea, I., Sanchez-Lozano, M., 2021. Design of porthole aluminium extrusion dies through mathematical formulation. Mater. Today Commun. 27, 102301.
[17] Zhang, C., Zhao, G., Chen, H., Guan, Y., Kou, F., 2012. Numerical simulation and metal flow analysis of hot extrusion process for a complex hollow aluminum profile. Int. J. Adv. Manuf. Technol. 60, 101–110.
[18] L.D.I. Dajda, Z.D.I. Hranos, Z.D.I. Petrzela, Extrusion of pipe bends and elbows - by means of die with eccentric hole and eccentrically mounted mandrel, in, Germany, 1978.
[19] Kowalik, M., Paszta, P., Trzepieciński, T., Kukiełka, L., 2021. Non-symmetrical direct extrusion. In: Analytical Modelling, Numerical Simulation and Experiment. Materials.
[20] Min, F., Zhu, G., Yue, B., Wang, Z., Yang, Z., Zhai, X., 2020. Influence of exit velocity distribution on self-bending extrusion. Eng. Res. Express 2, 015033.
[21] Min, F., Liu, H., Zhu, G., Chang, Z., Gao, X., Yue, B., Guo, N., Zhai, X., 2021. Self-bending extrusion molding of distorted channels. J. Mech. Sci. Technol. 35, 1945–1953.
[22] Valberg, H., 2002. Extrusion welding in aluminium extrusion. Int. J. Mater. Prod. Technol. 17, 497–556.

[23] Lu, X., Yu, J., Yardley, V.A., Liu, H., Shi, Z., Lin, J., 2021. Solid-state welding and microstructural features of an aluminium alloy subjected to a novel two-billet differential velocity sideways extrusion process. J. Mater. Process. Technol. 296, 117189.
[24] Xu, X., Zhao, G., Yu, S., Wang, Y., Chen, X., Zhang, W., 2020. Effects of extrusion parameters and post-heat treatments on microstructures and mechanical properties of extrusion weld seams in 2195 Al-Li alloy profiles. J. Mater. Res. Technol. 9, 2662–2678.
[25] Lu, X., Zhang, C., Zhao, G., Guan, Y., Chen, L., Gao, A., 2016. State-of-the-art of extrusion welding and proposal of a method to evaluate quantitatively welding quality during three-dimensional extrusion process. Mater. Des. 89, 737–748.
[26] Donati, L., Tomesani, L., 2008. Seam welds modeling and mechanical properties prediction in the extrusion of AA6082 alloy. Key Eng. Mater. 367, 125–136.
[27] Yu, J., Zhao, G., Cui, W., Chen, L., Chen, X., 2019. Evaluating the welding quality of longitudinal welds in a hollow profile manufactured by porthole die extrusion: experiments and simulation. J. Manuf. Process. 38, 502–515.
[28] Gagliardi, F., Citrea, T., Ambrogio, G., Filice, L., 2014. Influence of the process setup on the microstructure and mechanical properties evolution in porthole die extrusion. Mater. Des. 60, 274–281.
[29] Donati, L., Tomesani, L., Minak, G., 2007. Characterization of seam weld quality in AA6082 extruded profiles. J. Mater. Process. Technol. 191, 127–131.
[30] Zhang, C., Wang, C., Zhang, Q., Zhao, G., Chen, L., 2019. Influence of extrusion parameters on microstructure, texture, and second-phase particles in an Al-Mg-Si alloy. J. Mater. Process. Technol. 270, 323–334.
[31] Fu, L., Wu, G., Zhou, C., Xiu, Z., Yang, W., Qiao, J., 2021. Effect of microstructure on the dimensional stability of extruded pure aluminum. Materials.
[32] Sakai, T., Belyakov, A., Kaibyshev, R., Miura, H., Jonas, J.J., 2014. Dynamic and post-dynamic recrystallization under hot, cold and severe plastic deformation conditions. Prog. Mater. Sci. 60, 130–207.
[33] Yang, Q., Deng, Z., Zhang, Z., Liu, Q., Jia, Z., Huang, G., 2016. Effects of strain rate on flow stress behavior and dynamic recrystallization mechanism of Al-Zn-Mg-Cu aluminum alloy during hot deformation. Mater. Sci. Eng.: A 662, 204–213.
[34] Huang, K., Logé, R.E., 2016. A review of dynamic recrystallization phenomena in metallic materials. Mater. Des. 111, 548–574.
[35] Guo-Zheng, Q., 2013. Characterization for dynamic recrystallization kinetics based on stress-strain curves. Recent Dev. Study Recryst. 61–64.
[36] Lin, Y., Zheng, Z., Li, S., Kong, X., Han, Y., 2013. Microstructures and properties of 2099 Al-Li alloy. Mater. Charact. 84, 88–99.
[37] Fan, X.H., Tang, D., Fang, W.L., Li, D.Y., Peng, Y.H., 2016. Microstructure development and texture evolution of aluminum multi-port extrusion tube during the porthole die extrusion. Mater. Charact. 118, 468–480.
[38] Kaneko, S., Murakami, K., Sakai, T., 2009. Effect of the extrusion conditions on microstructure evolution of the extruded Al–Mg–Si–Cu alloy rods. Mater. Sci. Eng. A 500, 8–15.
[39] Chen, X., Zhao, G., Liu, G., Sun, L., Chen, L., Zhang, C., 2020. Microstructure evolution and mechanical properties of 2196 Al-Li alloy in hot extrusion process. J. Mater. Process. Technol. 275, 116348.
[40] Chen, Y., Yu, J., Ge, X., Sun, Y., Sun, L., Zhou, W., Zhao, G., 2024. Cryogenic deformation behavior, constitutive modeling and microstructure evolution of solution-treated 2195 Al–Li alloy at high strain rates. J. Mater. Res. Technol. 31, 2915–2929.
[41] Dong, Y., Zhang, C., Zhao, G., Guan, Y., Gao, A., Sun, W., 2016. Constitutive equation and processing maps of an Al–Mg–Si aluminum alloy: determination and application in simulating extrusion process of complex profiles. Mater. Des. 92, 983–997.
[42] Efunda Engineering Fundamentals: Aluminum. ⟨https://www.efunda.com/materials/elements/HC_Table.cfm?Element_ID=Al⟩; [Accessed 15 08 2024].
[43] Narvan, M., Ghasemi, A., Fereiduni, E., Kendrish, S., Elbestawi, M., 2021. Part deflection and residual stresses in laser powder bed fusion of H13 tool steel. Mater. Des. 204, 109659.
[44] Totten, G.E., MacKenzie, D.S., 2003. Handbook of aluminum. In: Physical Metallurgy and Processes, 1. CRC Press.
[45] Kaufman, J.G., 2018. Properties of pure aluminum[1]. Aluminum Science and Technology. ASM International.
[46] Long, B.T., Cuong, N., Phan, N.H., Toan, H.A., Janmanee, P., 2015. Enhanced material removal rate and surface quality of H13 steel in electrical discharge machining with graphite electrode in rough machining. Int. J. Sci. Eng. Technol. 4, 101–106.
[47] Levanov, A.N., 1997. Improvement of metal forming processes by means of useful effects of plastic friction. J. Mater. Process. Technol. 72, 314–316.
[48] Yu, J., Zhao, G., Chen, L., 2016. Analysis of longitudinal weld seam defects and investigation of solid-state bonding criteria in porthole die extrusion process of aluminum alloy profiles. J. Mater. Process. Technol. 237, 31–47.
[49] Chen, X.-M., Lin, Y.C., Wen, D.-X., Zhang, J.-L., He, M., 2014. Dynamic recrystallization behavior of a typical nickel-based superalloy during hot deformation. Mater. Des. 57, 568–577.
[50] Chen, G., Chen, L., Zhao, G., Lu, B., 2017. Investigation on longitudinal weld seams during porthole die extrusion process of high strength 7075 aluminum alloy. Int. J. Adv. Manuf. Technol. 91, 1897–1907.
[51] Xing, J., Alsarheed, M., Kundu, A., Coulter, J.P., 2022. Internal flow optimization in a complex profile extrusion die using flow restrictors and flow separators. Int. J. Adv. Manuf. Technol. 119, 4939–4950.
[52] Li, H., Huang, Y., Liu, Y., 2023. Dynamic recrystallization mechanisms of as-forged Al–Zn–Mg-(Cu) aluminum alloy during hot compression deformation. Mater. Sci. Eng. A 878, 145236.
[53] Wang, Y., Liu, Y., Zheng, J.-H., Lan, B., Jiang, J., 2022. Develop a new strain rate sensitive solid-state pressure bonding model. Mater. Des. 215, 110436.